The Pleiades Reflection Nebula. I. Ultraviolet, Optical, and Far-Infrared Imaging Photometry

Steven J. Gibson[1], Kenneth H. Nordsieck[2]

ABSTRACT

We present new wide-field optical and ultraviolet images of the Pleiades reflection nebula that allow a more thorough evaluation of the dust scattering than any prior data set. Vacuum-UV images were taken at 1650 & 2200 Å during the first flight of the *Wide-field Imaging Survey Polarimeter*, a sounding rocket borne telescope. *WISP* captured the brighter parts of the nebula at both wavelengths, with 3σ sensitivities of 22.5 & 23.4 UV mag arcsec^{-2}, respectively. The $5^\circ \times 1.^\circ 7$ *WISP* field was also mapped at 4400 Å with a mosaic of 40 Burrell Schmidt CCD frames using a broadband B_J filter. The Schmidt mosaic shows extensive and intricate nebulosity down to a 5σ sensitivity limit of 27.6 B mag arcsec^{-2}, including features undetected by photographic surveys.

We explore the intensity and color behavior of the nebula in our UV and optical images and far-infrared *IRAS* data. We find the photometric structure near bright stars is more complex than previous studies have implied, but general trends are still apparent. The color gradients around the stars are caused by phase function effects rather than internal reddening. The greater concentration of scattered light vs. thermal emission indicates that most of the observed scattering is from foreground dust. A somewhat greater concentration of UV vs. optical light suggests grain scattering is more forward-directed at shorter wavelengths. The UV nebula is much fainter than expected from the stellar photometry and interstellar reddening. Explaining this UV faintness requires either more reddening than is measured or significant alterations to current dust property estimates.

Subject headings: scattering — techniques: image processing — (ISM:) dust, extinction — ISM: individual (Pleiades) — (ISM:) reflection nebulae — ultraviolet: ISM

---

[1]Dept. of Physics & Astronomy, University of Calgary, 2500 University Drive N.W., Calgary, Alberta T2N 1N4, Canada; gibson@ras.ucalgary.ca

[2]Dept. of Astronomy, University of Wisconsin, 475 N. Charter St., Madison, WI 53706; khn@sal.wisc.edu

1. Introduction

The brightness and color distributions of reflection nebulae are functions of their three-dimensional structure and dust scattering properties. In principle, the dust behavior and nebular geometry can both be extracted from a photometric analysis, but in practice, separating the two is difficult without detailed, reliable photometry and significant external constraints. This problem is especially challenging in the far-ultraviolet, where the complexity of the observations (e.g., Bowyer 1991; Henry 1991) and paucity of constraints have lead to major disagreements over dust properties (e.g., Hurwitz, Bowyer, & Martin 1991; Witt et al. 1992).

The *Wide-field Imaging Survey Polarimeter* (*WISP*; Nordsieck & Harris 1999) was built to determine 3-D geometry polarimetrically via the simple, Rayleigh-like polarization phase function of the dust (White 1979) and then calibrate its UV intensity phase function. The first three *WISP* targets were the Pleiades reflection nebula (Gibson 1997), the Large Magellanic Cloud (Cole et al. 1999; Cole, Wood, & Nordsieck 1999), and Comet Hale-Bopp (Harris et al. 1999). Polarimetry was not obtained for the Pleiades due to noise problems and an unexpectedly faint UV nebula, but other constraints have allowed a scattering analysis to proceed.

The Pleiades nebula (e.g., Figs. 7 & 8) was selected for the current study for several reasons. It is a large, bright, nearby object ($d \sim 130$ pc; Stello & Nissen 2001), allowing dust to be observed for a variety of scattering angles. Photometric measurements are unlikely to be contaminated by line emission, since absorption studies of the region show only low ionization species (White 1984; Trapero et al. 1996), the Hα emission is very weak (S. Tufte 1993, private communication), and neither fluorescent emission nor extended red emission are found (Rush & Witt 1975; Witt & Boroson 1990). Finally, the scattering geometry is constrained by a wealth of observations.

Interstellar polarization and reddening (e.g., Breger 1986, 1987), atomic and molecular line absorption (Federman 1982; Bohlin et al. 1983; White 1984; White et al. 2001), radio line emission (Gordon & Arny 1984; Federman & Wilson 1984; Bally & White 1986), and far-infrared thermal emission (Castelaz, Sellgren, & Werner 1987; White & Bally 1993) indicate a low level of interstellar matter across most of the cluster but more on the western side, perhaps with some optically thick dust southwest of the star 23 Tau (Merope). Enough material is probably in front of the major stars to dominate the scattered light budget for forward-scattering grains, but some of the densest gas and dust may lie behind or among the stars on the west side of the cluster. These findings are more recent than most photometric studies, which have reported conflicting geometries of dust-behind-star (e.g., O'Dell 1965; Greenberg & Roark 1967; Andriesse, Piersma, & Witt 1977), star-behind-dust (Schalén 1948;

Jura 1979; Witt, Bohlin, & Stecher 1986), and star-within-dust (Greenberg & Hanner 1970; Witt 1985). The disagreement is partly due to these studies' focus on the brightest, most complex nebulosity on the west side of the cluster, but it also highlights the importance of external constraints.

Our scattering investigation uses optical and UV scattered light photometry with far-infrared (FIR) emission measurements to constrain dust and geometric models, as originally suggested by Jura (1977). Unlike the common circumstellar case, the Pleiades nebula's analysis is simplified by its foreground geometry and low reddening, which reduce sightline confusion: if the thermal and scattered light sample the same grains, a ratio of the two will remove density structure and leave only scattering effects. This paper presents our multiwavelength photometry. We discuss data processing and reliability issues first (§§2-5) and then consider implications of the nebula's intensity and color behavior near several bright stars (§§6-7). Detailed model analyses are given in a companion paper (Gibson & Nordsieck 2003; hereafter Paper II).

2. *WISP* UV Data

2.1. Observations

The *Wide-field Imaging Survey Polarimeter* (*WISP*; Nordsieck et al. 1994; Nordsieck & Harris 1999) is a sounding rocket borne telescope designed to obtain the first wide-field polarimetric images in the vacuum ultraviolet. Instrumental optics project a $5.^{\circ}0 \times 1.^{\circ}7$ field onto a Reticon 1200×400 CCD, providing $14.''9$ per 27μm pixel. Two broadband filters, W_1 and W_2, cover a wavelength range of $1350 - 2600$ Å, with respective half-power bandpasses of 1650 ± 250 and 2200 ± 300 Å. The telescope is a fast, folded, off-axis Schmidt design with polarizing and modulating elements. The modulator, a stressed CaF_2 waveplate, sets the effective aperture of 19cm. Subsequently, the light reflects off a Schmidt corrector mirror, a Brewster-angle ZrO_2-coated polarizer, and the $F/1.8$ primary mirror, and then passes through a field flattener and UV filter to reach the CCD.

The Pleiades field, shown in Figures 1 & 2, covers the bright inner nebula and part of the outer nebulosity to the northeast, though the latter proved too faint for detection. *WISP* was launched from White Sands, New Mexico just after midnight on 1994 December 3. Half of the 15 minute flight was spent above an altitude of 120 km, where atmospheric airglow and UV attenuation are minimal; the peak altitude was 300 km. Four 35 second images measured the Stokes intensities Q^-, Q^+, U^-, and U^+ (orientations of -90°, $+0^{\circ}$, -45°, and $+45^{\circ}$) in each filter, and pixels were binned 2×2 on-chip to increase sensitivity. The pointing

stability was $< 0\farcm5$ along the short axis of the images, but a small jitter blurred stars $\pm1'$ in the long-axis direction. The field center also shifted $21\farcm6$ west and $4\farcm5$ south of the planned position to [2000] $3^h48^m34^s$ $+24°41'13''$, but since most of the detected UV nebulosity is near the cluster center, this shift does not affect our results.

2.2. Initial Reduction

Bias structure was removed from each flight exposure by subtracting an average of zero-time exposures taken before and during the mission. Bias levels drifted in flight and were not recorded, but they were recovered as 3σ-clipped median levels in apparently empty areas of dark-subtracted images. The dark structure was found from an average of bias-subtracted dark frames, and the dark current in each 35-second Pleiades exposure was 24.0 ± 4.9 electrons per 2×2 binned pixel, with some spatial structure at the level of a few e^-. The chip readout noise was 10.4 e^-. Flatfield corrections were not possible, but atmospheric backgrounds were absent, and flux calibration measurements indicate the chip response varied by a few percent or less within the region of usable photometry.

The flux calibration compared observations of 17, 18, 20, & 23 Tau to *TD-1* fluxes (Thompson et al. 1978) linearly interpolated to *WISP* filter wavelengths. Since the total intensity $I \equiv Q^- + Q^+ \equiv U^- + U^+$, we measured the integrated counts of each star as half the total flux from all four polarization exposures within a $10'$ box centered on the star. The large box size was needed to capture the majority of each star's light, which was smeared out in a broad and complex point spread function (PSF; Fig. 3). Though sharp nebular features were blurred by the PSF, many of these were too faint to detect without considerable smoothing. The standard deviation of the ratio of *WISP* and *TD-1* stellar fluxes indicates internal calibration errors of $\leq 4\%$, which is much smaller than the $\sim$20% absolute uncertainty of the *TD-1* dataset. The PSF subtractions below have similarly high internal consistency; our absolute photometric errors are probably dominated by systematic uncertainties from the *TD-1* catalog or from PSF removal.

2.3. Point Spread Function Removal

The *WISP* PSF contamination near bright Pleiades stars often exceeds the nebular brightness and so must be removed. Telescope PSFs typically have a bright core and a faint outer *aureole* that fades with angular offset ϕ as ϕ^β, where $-1 \gtrsim \beta \gtrsim -3$ (King 1971; Kormendy 1973; Racine 1996). *WISP*'s off-axis optics and problems with in-flight focus and

pointing stability produced a complex PSF core (Fig. 3) but a fairly simple aureole with $-1.3 \geq \beta \geq -2$ over $5' \leq \phi \leq 60'$ (Fig. 4); small field flatness problems appear for $\phi \gtrsim 1^\circ$ at levels below the photometric noise. Common PSF removal methods (e.g., DAOPHOT: Stetson 1987) fit a 2-D Gaussian function and residual map to a measured stellar PSF, scale this model to various stars, and subtract it. But since the *WISP* PSF has neither a well-behaved core nor a negligible aureole, a complete 2-D map of the PSF over the entire field was used instead.

Laboratory W_2 test lamp images were used for both W_1 and W_2 aureoles, with appropriate convolutions to simulate the pointing jitters recorded by in-flight telemetry; W_1 lab images were not available. The lab PSF cores match the in-flight appearance of stars poorly, so the $10' \times 10'$ core was taken from appropriately scaled star images for each filter and Stokes component. The grafting process worked well for the W_2 core but was less successful with the W_1 core. The stellar core in each exposure was taken from the brightest Pleiad, 25 Tau, with checks against fainter stellar cores to remove cosmic ray contamination. Bright noncluster stars were not observed, but 25 Tau is relatively isolated from other bright stars' PSF wings and has little heavy nebulosity. Its core width at half maximum is $\sim 1\farcm25 \times 2\farcm5$, which we adopt as the *WISP* resolution before smoothing.

We removed the stellar PSFs with a modified version of the classic CLEAN algorithm (Högbon 1974). All bright stars were located by cross-correlating against the 25 Tau core map and eliminating cosmic ray misidentifications. Then the model PSF was centered on the currently brightest star, scaled to 10% of its flux, and subtracted; the scale value was stored and the process repeated until all scales converged. To accommodate subpixel positioning, the PSF structure was fit and resampled with a logarithmic bi-cubic spline. Position dependence in the real PSF core's shape led to nonzero residuals in stellar cores, but the subpixel centering improved aureole subtraction. A subsequent check of the PSF-subtracted *WISP* data against external photometry (§4) validated the W_1 intensities but found a 40% oversubtraction of the W_2 PSF, which was re-added. With this correction, the *WISP* intensities match the external data within 1σ uncertainties, apart from PSF core areas within a few arcminutes of bright stars.

2.4. Final Steps

Since the nebula proved too faint for polarimetry, total-intensity maps were produced by averaging the Q & U frames together with cosmic-ray rejection statistics. The total intensity maps have 3σ sensitivities of 2.7 and 1.1×10^{-17} erg cm^{-2} s^{-1} Å^{-1} arcsec^{-2} for W_1 and W_2, respectively. This was improved by median smoothing each image with 3σ-clipping

and the stellar cores masked out. To avoid unnecessary smoothing of small-scale features, we extracted our photometry from unsmoothed images as well as those smoothed with $1\farcm5\times1\farcm5$ and $3\farcm5\times3\farcm5$ windows, and the least-smoothed data with an acceptable S/N ratio were used. The most-smoothed data have 3σ levels of 3.5 and 1.5×10^{-18} erg cm^{-2} s^{-1}Å^{-1}arcsec^{-2}, or 22.5 and 23.4 UV mag arcsec^{-2} in the convention of Henry et al. (1988).

The completed images in Figure 5 reveal significant nebulosity. The stars 20 Tau (Maia), 23 Tau (Merope), and 25 Tau (Alcyone) have prominent nebular glows; the lack around 25 Tau in W_1 results from PSF core calibration problems. The stellar halos merge into a diffuse nebular glow like that seen in photographs, but the faint outer nebulosity remains undetected. The UV nebular intensities are generally less than might be expected from optical intensities and the UV brightness of the illuminating stars.

3. Schmidt Optical Data

3.1. Observations

To examine UV-optical colors, the *WISP* field was mapped with the 0.61m Burrell Schmidt telescope. The Schmidt's $F/3.6$ optics give a plate scale of $96\farcs6$ mm^{-1}, or $2\farcs03$ per unbinned 21 μm pixel on the S2KA Tektronix 2048×2048 CCD. At the time of the observations, the fields were vignetted into $67\farcm2$ circles by the filter holder. We used a B_J $3600-5200$ Å deep sky filter (Gullixson et al. 1995) to maximize sensitivity to the nebula, which has blue colors.

Figure 1 shows the 20 Schmidt field pairs used to map the *WISP* area. Observations were made during the nights of 1993 December $12-16$ & 18, which we denote as nights $1-5$ & 7. The target priority favored the faint outer nebulosity east of the cluster core. Each field was exposed for 1000 seconds and offset from its twin to shift bad pixels. The long integrations caused pixel saturation around the bright stars but helped overcome the S2KA's read noise of 13 e^- and minimized read time overhead. Sensitivity was also improved by binning pixels 2×2 on the detector.

3.2. Initial Reduction

Bias levels were measured from overscans and subtracted, as was bias structure in an average map of 105 zero-time frames. The dark structure was too small to subtract given its uncertainties. The few bad pixels in the S2KA chip were interpolated over with neighbor

values, as were saturation bloom columns for the bright stars. The latter were distinguished from saturation disks around the same stars with pattern-recognizing software; the disks, which have intensities exceeding 19.2 B mag arcsec^{-2}, were left in place.

Fields were flattened in a two-stage process. First, the images were divided by a normalized median combination of 16 twilight exposures to remove the basic instrumental response. Significant structure was left due to the color difference between the blue twilight sky and the yellow zodiacal light dominating the "dark" sky near the Pleiades (Levasseur-Regourd & Dumont 1980; Schoening 1992). As a second correction, each field was divided by a 3σ-clipped median average of 13 dark-sky fields taken away from the cluster during nights 1 & 2. PSF wings and saturated pixels were removed and faint stars masked in each of these sky frames prior to combination, and remaining artifacts were eliminated with a $3\farcm4\times3\farcm4$ median smooth of the combined map.

The first two nights were clear with a new moon, but cirrus appeared later, scattering waxing moonlight into the Schmidt aperture. This contamination was significant for nights 4 & 5 and strongest for night 7, though the latter's fields were in less important parts of the nebula. Smooth moonlight corrector maps were constructed in a similar manner to the dark sky flat, using 10 night 4 & 5 skies for one map and 5 night 7 skies for another. After these were subtracted from the Pleiades frames, east-west gradients equivalent to 17% of new moon B sky per degree in nights 4 & 5 and 22% in night 7 were measured visually and removed. Remaining gradients and the sky zero-level were fine-tuned with field overlaps during mosaic assembly.

The flux calibration used 12 Landolt (1972) standard stars observed over nights 1 & 2 when conditions were best. No color transformation was needed between B_J and B, which have the same center wavelength. The absolute uncertainty of the calibration is $\sim$8% plus $6-10$% from extinction uncertainties over the range of observed airmasses. The relative uncertainty between frames is less than 5% with flatfield errors included. The flux scale after calibration is for zero airmass.

3.3. Point Spread Function Removal

As with *WISP*, stellar PSF wings were often brighter than the nebula and required careful removal. But in this case, the PSF core was inside the saturation disks, and the PSF aureole could be reasonably represented as a simple 1-D radial function. Figure 6 shows the measured profile and power-law fit. The profile was obtained from the 7th-mag A5 star HD 15333 in night 1 dark-sky frames using the median of the lowest 10% of pixel values

in successive annuli. This statistic avoids most contamination from neighbor star aureoles, diffraction spikes, and other artifacts. The measured profile conforms to a power-law shape out to offsets of $\phi \sim 15'$, where field edge effects begin interfering. We fit a $\beta = -1.67$ law to the profile minima in this range to minimize residual artifacts and extrapolated it to $\phi \leq 60'$ to remove PSF aureoles from each Schmidt field. PSF subtraction was performed on fields rather than the mosaic because vignette and scattered light effects made aureoles discontinuous across field boundaries.

Since the Schmidt PSF cores of bright stars were saturated, a CLEAN-like algorithm could not be used to remove them. Instead, the power-law aureole was scaled to the catalog magnitude of each saturated star and removed; unsaturated stars were too faint ($B \gtrsim 11.5$) to have significant aureoles. For dark sky images used to make sky flats and moonlight corrections (§3.2), the stellar profiles had no nebular component and could be measured and removed directly. A comparison of our final maps against previous photometry (§4) shows excellent agreement except in the innermost few arcminutes, where some PSF residuals may remain.

3.4. Mosaic Assembly

All the Schmidt Pleiades fields were assembled into a single mosaic of weighted average intensities. Pixels near field edges were given low weight to reduce flatfield and scattered moonlight residuals in these areas, and the lowest 20% and highest 40% of pixel values were clipped to minimize other artifacts. The fields were placed on the mosaic grid after each was registered against stellar catalog positions from Röser & Bastian (1988).

The mosaic process also allowed sky backgrounds to be adjusted to a common level. In an iterative procedure, the relative DC levels of overlapping fields were set to minimize root-mean-square (RMS) differences between pixels avoiding stars and various artifacts, the field mosaic was assembled, and residual scattered moonlight gradients were measured globally and removed from each field. The tendency of the overlapping field gradients to join into global patterns made them easy to fine-tune at this stage. Visual checks against Palomar Observatory Sky Survey prints reduced gradient uncertainties below those of field edge matches, which are typically 26.2 B mag arcsec^{-2} = 4% of sky or less but can reach 12% in the worst cases (see Fig. 6). These uncertainties limit the reliability of the largest faint features but have no affect on small filaments. Once all gradients were removed, the global sky level of the mosaic was set by assuming the faintest areas free of nebulosity have zero intensity. Since this method is blind to structure larger than the mosaic, our photometry may underestimate the total nebular brightness, but the bias should be less than the 1σ

errors on our external photometry check, which are $\sim$25.6 B mag arcsec^{-2} = 7% of sky (§4).

After the mosaic assembly was completed, neighbor interpolation was used to remove a number of long, thin streaks of light scattered by the filter holder edges, as these could otherwise contaminate photometric measurements. A few defocused ghost images of bright stars were too extended and complex to remove, but these are quite faint ($\gtrsim$ 26 B mag arcsec^{-2}).

Figures 7 & 8 show the final map. Intricate filaments fill the mosaic; some, like the horizontal streamers in the southernmost field, are below the POSS detection limit. All features found by *WISP* are easily seen here. Without binning, the mosaic's 5σ sensitivity is 1.0×10^{-18} erg cm^{-2} s^{-1}Å^{-1}arcsec^{-2} = 24.5 B mag arcsec^{-2}. Binning to *WISP*-like 30″ pixels improves the 5σ sensitivity to 6.0×10^{-20} erg cm^{-2} s^{-1}Å^{-1}arcsec^{-2} = 27.6 B mag arcsec^{-2}, or $\sim$1% of sky for small-scale features, though larger structures are compromised by field edge artifacts at the $25 - 26$ B mag arcsec^{-2} level.

The detected nebula ranges over three orders of magnitude in surface brightness. Near 20, 23 & 25 Tau, intensities exceed μ_B = 20.4 mag arcsec^{-2}. The nebulosity near 23 Tau drops to 22.1 at $\phi = 15'$ and to 22.9 at 40′, where it blends into the general cluster nebula. This has $\mu_B = 22.1 - 22.9$ inside the quadrilateral of 17, 20, 23 & 25 Tau and falls to 25.0 at $\phi \sim 1°$, where it appears to merge with several other structures having $\mu_B = 24.2 - 25.4$. Arcminute-scale wisps are visible within these larger features with intensities of 27.6 B mag arcsec^{-2} above local background.

4. Comparison with Previous UV and Optical Photometry

As a check on our processing techniques, we compared our final data with external UV and optical aperture photometry. No imaging photometry of the Pleiades nebula has been published in detail, though *Midcourse Space Experiment* observations were reported by Allen et al. (1997). We used the 14 UV pointings of Andriesse et al. (1977; APW) and the 6 optical pointings of O'Dell (1965), all near the star 23 Tau (Merope). Though their respective apertures of 150″ and 63″ differ from our own resolution, diffuse surface brightness measurements should be unaffected. Other studies were not considered, since Witt et al.'s (1986) UV data sample too close to the stars, Elvius & Hall (1967) are consistent with O'Dell (1965), and optical data around other stars (e.g., Cottrell & Witt 1983; O'Dell 1969) lack matching UV coverage.

We assumed no stellar PSF contamination in the reference data. A study of the instrument used by APW found minimal PSF contamination (A. Witt 1998, private communication; Wesselius 1980), and O'Dell (1969) made a similar claim for the O'Dell (1965)

photometry. Witt (1977) sought to remove 23 Tau's optical aureole explicitly but found values at least as bright as O'Dell's (1965) for $\phi \gtrsim 3'$.

Figure 9 compares our photometry to the reference data, with ours taken from the pixels containing the reference positions. The *WISP* data at $\phi \gtrsim 8'$ were extracted from $1\farcm5 \times 1\farcm5$-smoothed images, except for the outermost W_1 point, which used $3\farcm5 \times 3\farcm5$ smoothing. Three W_1 and two W_2 points within $\phi \sim 3'$ have large PSF residuals and fall outside the plotted intensity range. We interpolated the reference data in wavelength for this comparison, and the APW intensities were increased by 8% to match the *TD-1* flux scale, but the data are unaltered otherwise. The dashed line marks APW's power-law fit to the Merope nebula, which we discuss more in §6.

The general agreement between our photometry and the reference sets validates our elaborate reduction procedures. Only the innermost offsets show discrepancies. *WISP* problems for $\phi \lesssim 3'$ have been discussed (§2.3). A $\sim$25% overbrightness for similar offsets in the Schmidt data suggests imperfect PSF subtraction here as well. We note that the general UV match is not a consequence of using APW to calibrate the *WISP* PSF subtraction (§2.3), since this is only a global scaling correction; the detailed agreement vs. ϕ is genuine.

5. Far-Infrared Data

5.1. *IRAS* Emission

A comparison of isotropic thermal radiation and anisotropic scattered light is useful for examining dust phase function effects. Our primary FIR data are from *IRAS* Sky Survey Atlas (ISSA; Wheelock et al. 1994) maps at 60 & 100 μm. Large grains dominate the emission at these wavelengths (Castelaz et al. 1987) and should also dominate the scattered light, due to the steep dependence of scattering cross-section on particle size in the Rayleigh limit (van de Hulst 1981). The ISSA $\sim 5'$ angular resolution is similar to *WISP*'s after $3\farcm5 \times 3\farcm5$ smoothing. The ISSA data contain some striping and background matching artifacts, but these have amplitudes below 1 MJy sr^{-1} and can be ignored. A more serious concern is the ISSA zero-point uncertainty of a few MJy sr^{-1}. We subtracted 4.8 MJy sr^{-1} from the ISSA 100 μm data to match the *COBE*-calibrated *IRAS* maps of Schlegel, Finkbeiner, & Davis (1998; SFD) within a $\pm$0.6 MJy sr^{-1} RMS uncertainty. Lacking a similar reference for 60 μm, we added 0.7 MJy sr^{-1} to bring the faintest real-looking ISSA nebulosities up to zero intensity. The 100 μm zero-point changes have a large effect on outlying features but only $5-25$% in the central regions where *WISP* detected the nebula. The smaller 60 μm correction has no significant effect beyond making temperature measurements possible

in faint areas.

Figure 10 shows a map of zero-corrected 100 μm intensities from the *SkyView* imaging engine (McGlynn, Scollick, & White 1996). As noted by Castelaz et al. (1987) and White & Bally (1993), the FIR nebula is similar to the scattered light nebula. Bright thermal glows mark 17, 20, 23, and 25 Tau, but the brightest emission is from the dense nebulosity southwest of 23 Tau. Many faint extended features have optical counterparts (Fig. 8). Contours give 60/100 μm color temperature T. We assume $I_\nu \propto \kappa_\nu B_\nu(T)$ with Planck function $B_\nu(T)$, volume opacity $\kappa_\nu \propto \nu^\alpha$, and SFD's $\alpha = 2$; general constraints are $1 \leq \alpha \leq 2$ for $50 \leq \lambda \leq 250$ μm (Hildebrand 1983; Whittet 1992). We find $T \sim 18 - 36$ K over the nebula, or $20 - 45$ K if $\alpha = 1$. Our 60/100 μm temperatures are 25% higher than SFD's *COBE* 100/240 μm values in the warmest regions (§5.2), perhaps due to some small grain emission at 60 μm. The uncertainties in our data from small-grain emission, zero-point corrections, and the choice of α are probably similar to the uncertainty in the *IRAS* gain. All these effects may bias our analyses somewhat but should have no qualitative impact.

5.2. Longer Wavelengths

The main disadvantage of *IRAS* is its short wavelength coverage of $8 - 120$ μm, which sees only the Wien side of the Planck function for grains cooler than ~ 50 K. By contrast, the *COBE* DIRBE and FIRAS instruments cover $1 - 240$ and $104 - 4400$ μm respectively, or temperatures of $\gtrsim 20$ K and $\gtrsim 1.2$ K on their larger beam scales of $0.^\circ7$ and 7°. To check our 60/100 μm color temperatures and the possibility that *IRAS* missed a colder dust population, we examined DIRBE and FIRAS temperature data near the Pleiades.

SFD produced DIRBE 100/240 temperature maps at $1.^\circ3$ resolution. Little small-grain emission is expected for $\lambda \gtrsim 100$ μm, and SFD treated zodiacal contamination carefully, so their temperatures are probably more reliable than ours on these scales. When derived from ISSA maps smoothed to a similar resolution, our 60/100 temperatures $2 - 3^\circ$ from the cluster center are $14 - 16$ K, in good agreement with SFD. In the cluster core however, our $25 - 26$ K peak temperatures exceed SFD's $20 - 21$ K values, suggesting some small grain contamination.

Reach et al. (1995) analyzed FIRAS data and found that Galactic dust emission in Taurus is dominated by a $T \sim 17$ K component, which is consistent with ISSA and DIRBE temperatures near the Pleiades. Reach et al. (1995) also found evidence for a weak $T \sim 5$ K component that *IRAS* would have missed, but this was not confirmed by Lagache et al. (1998). If real, this second component produces less than 2% of the emission power of the

dominant component, suggesting its scattering contribution may also be small. We have not considered the effects of such a population in our analyses.

6. Intensity Behavior

The behavior of the nebular brightness I_λ as a function of apparent angular offset ϕ from bright stars depends upon the 3-D positions of the stars and dust. We examine $I_\lambda(\phi)$ below for 17, 20, 23, and 25 Tau at 1650 Å, 2200 Å, 4400 Å, and 100 μm. Color trends are explored in §7.

6.1. Profile Data

Figure 11 shows the "domains" of different stars illuminating the nebula at 4400 Å, assuming all stars and dust lie in a single plane normal to the line of sight. Contours indicate how much of the model illumination comes from a particular star. This simple scheme gives a rough idea of where the nebula is dominated by one star, and thus where extracted intensity profiles might be physically meaningful. But since the real geometry probably differs from this model, the contribution fractions implied by the model should not be taken too literally. We chose to examine $I_\lambda(\phi)$ at model contribution levels below 50%, recognizing that starlight blending is significant in the Pleiades (Jura 1979), and $I_\lambda(\phi)$ will be affected by it.

Figure 12 gives the extracted profiles in order of decreasing interstellar reddening, a proxy for nebular optical depth. We measured $I_\lambda(\phi)$ at contribution levels of $\geq 25\%$ for 17 & 25 Tau, $\geq 15\%$ for 20 Tau, and $\geq 10\%$ for 23 Tau; 20 & 23 Tau have lower cutoffs to give them areas similar to 17 & 25 Tau. No azimuthal averaging was performed. Profiles are shown for all position angles ψ around the star and for ψ subsets that minimize starlight blending and nebular structural variations where possible; we define $\psi = 0^\circ$ as north and $\psi = 90^\circ$ as east.

Some quantization appears in both the UV and FIR profiles. The latter is caused by pixel edge discontinuities in the ISSA data, while the former is a result of *WISP* smoothing to increase sensitivity. To avoid washing out bright, small-scale features, the *WISP* photometry at each position was extracted from the least-smoothed data satisfying $S/N \geq 5$ (§2.4). Since the smoothed data were more sparsely sampled to avoid redundant points, abrupt drops in point density in the UV profiles appear where the degree of smoothing increased. Points with $S/N < 5$ for maximum smoothing are not plotted, truncating most *WISP* profiles at

$\phi \sim 20 - 30'$. Points with $\phi < 4'$ had PSF subtraction problems and are also omitted.

The relative 4400 Å and 100 μm photometric uncertainties are too small to plot in Figure 12, and the UV error bars cannot be shown properly for so many points. But for reference, the 1650 Å 1σ uncertainties range from 9.0×10^{-18} erg cm^{-2} s^{-1}Å^{-1}arcsec^{-2} for the inner, unsmoothed points to 1.2×10^{-18} for the outer, heavily smoothed points. The corresponding 2200 Å range is 3.7 to 0.5×10^{-18} erg cm^{-2} s^{-1}Å^{-1}arcsec^{-2}.

6.2. Profile Behavior

6.2.1. General Characteristics

The nebular intensity profiles in Figure 12 have several common characteristics. Nearly all show I_λ dropping steadily at larger offsets, as expected from the local dominance of the reference stars. Exceptions arise from *WISP* PSF artifacts and optical depth variations in the nebula. One example of the latter is the strong 100 μm peak $10'$ from 23 Tau, which appears in more than one star's profiles and traces significant molecular material (Breger 1987; White & Bally 1993). Another is the nebular "hole" northeast of 25 Tau (see Figs. 8 & 10). The general scatter in the profiles is reduced in the ψ subrange plots, demonstrating that it arises from structural effects, not noise. Aperture photometry studies of a few positions in the nebula present a simpler picture than our image data. A thorough scattering analysis should address the causes of this structure, such as optical depth variations.

APW's study provides an interesting comparison with our own. They combined UV data taken mostly south and west of 23 Tau with O'Dell's (1965) optical data of similar areas and found reasonable fits using the power-law form $I_\lambda(\phi) = I_\lambda(\phi_0) \cdot (\phi/\phi_0)^{\beta_\lambda}$, where $\beta_\lambda < 0$ and $|\beta_\lambda|$ steepens at shorter wavelengths. Thus, the Merope nebula is redder in its outer reaches, as color photographs indicate. We have plotted APW's power laws in Figure 12, scaled to each star's brightness and interpolated in wavelength. Though the APW lines are only fits to their data for 23 Tau itself, they aid the eye in comparing 23 Tau's intensity profiles to those of other stars.

Within the $2.25' < \phi < 13.57'$ offset range of the APW data, our 23 Tau profiles agree quite well with the APW fit lines, especially for the $180° < \psi < 225°$ azimuthal range of most of their pointings. But for $\phi \gtrsim 15'$, our profiles diverge considerably, perhaps because of optical depth effects or a drop below $\sim$30% contribution from 23 Tau. Other stars' profiles show similar behavior: 20 Tau matches the APW line well at small offsets but diverges from it more quickly than 23 Tau, while 25 and 17 Tau diverge further but often run parallel to the APW line. In most cases, the profiles' power-law behavior is more pronounced at smaller

offsets, where neighbor star illumination and nebular structure are less important. 23 Tau's profiles appear to be the brightest, which is consistent with its nebulosity being the heaviest.

6.2.2. Shallow Slopes

APW slopes interpolated to 1650, 2200, & 4400 Å are −1.47, −1.31, & −0.73, respectively. Though our profile slopes vary, none drops more steeply than $\beta_\lambda \sim -1.5$ except in short bursts (e.g., 23 Tau at 4400 Å). This result seems to contradict that of Hubble (1922), who found the angular extent of many reflection nebulae is proportional to the square root of the flux of the central star(s), implying $\beta_\lambda = -2$ profiles are common near nebular edges on the sky. Physically, a −2 slope is consistent with a simple inverse-square drop in illuminating flux from the center if the dust optical depth is low and phase function effects are minimized by near-constant $\sim 90°$ scattering angles. In the inner nebula, scattering angles would vary more, but this variation would steepen β_λ if foreground dust dominates the scattering in the Pleiades, as seems likely (§§1 & 7.1).

The shallow slopes are probably not caused by optically thick dust. Though smooth thick dust would alter the light distribution, it is incompatible with low interstellar reddenings (Breger 1986). The nebula's rich filamentary structure (e.g., Arny 1977) might hide extra opacity in small dust clumps, but it is not clear whether these could intercept enough light to affect profile slopes.

Other explanations are more plausible. A relatively large star-nebula separation would soften phase function effects by reducing changes in scattering angle over a given range of sky offsets. In a foreground-slab geometry, the incident flux would also vary less with ϕ in the inner nebula where the star-dust distance is more constant. Finally, the light contributions of neighbor stars to the outer parts of profiles would lessen the rate of decline, especially if the dust lies some distance in front of the stars, where the light can blend more evenly. Blending could also be significant in the outer nebula if much of the illumination is from the ambient interstellar radiation field. Paper II considers all of these effects on the scattered light distribution.

7. Color Behavior

We now consider the behavior of colors, defined as brightness ratios $I_{\lambda_1}/I_{\lambda_2}$. We discuss colors of scattered light relative to thermal emission first and then examine colors between different scattered light wavelengths.

7.1. Scattered / Thermal Colors

In an optically thin nebula, the ratio of scattered and thermal intensities cancels dust density structure and illuminating flux scalings to leave only phase function effects. Paper II examines such behavior in detail, but we mention some fundamental results here.

Figure 13 plots UV/FIR and optical/FIR ratio profiles using the azimuthal subrange data from Figure 12. Some *WISP* artifacts are present, and 1650 Å/100 μm colors are too affected by PSF residuals to show for 25 & 17 Tau. Still, most scattered/thermal ratios clearly drop with increasing offset angle ϕ. Ratios are $\sim 10^{-1} - 10^{-2}$ for $\phi \sim$ a few arcminutes and $\sim 10^{-3}$ at larger offsets. The latter value is typical of $B_J/100\mu$m ratios outside the cluster core area and resembles the optical/FIR colors of many high-latitude Galactic cirrus clouds (Guhathakurta & Tyson 1989; Paley et al. 1991; Guhathakurta & Cutri 1994), suggesting these outer nebulosities may receive much of their illumination from the diffuse interstellar radiation field.

The scattered/thermal color gradient directly implies that most of the scattered light comes from dust foreground to the illuminating stars, i.e., those within $\sim 1^\circ$ of the cluster center that dominate the nebular light, not all cluster stars inside the $\sim 6^\circ$ tidal radius (Adams et al. 2001). If we assume the scattered and thermal light trace the same grain population, and the nebula is optically thin, then the differences between the scattered and thermal intensity distributions show that the grains do not scatter isotropically. Since grains are not likely to backscatter preferentially (Whittet 1992), they must forward-scatter preferentially, and the higher scattered/thermal ratios near the stars require the bulk of the scattered light to arise from dust in front of the stars. Some dust could still lie in the background, but it does not dominate the scattering.

Several departures from our assumptions could complicate this line of reasoning, but none seriously. Optically thick smooth dust might produce similar gradients, but low interstellar reddening (Breger 1986) rules this out in most parts of the nebula. Optically thick dust clumps can only produce color gradients if they scatter off one another, which would also produce unobserved sightline reddening effects. Finally, complex-shaped grains might have backscattering components in predominantly forward-directed phase functions, and these could mimic the same color trends for a background nebula. But realistic fluffy-grain models have backscattered intensities less than 10^{-2} times that of light going forward (Wolff, Clayton, & Gibson 1998). If background dust dominated the scattered light, it would produce far more background extinction than is observed, even through the dense Merope cloud area (Černis 1987).

7.2. Scattered / Scattered Colors

Ratios of scattered brightness in different filters reveal dust property changes with wavelength. We discuss implications of these colors below.

7.2.1. Color Trends

Figure 14 plots scattered light intensity ratio profiles, with APW trends and stellar colors marked for comparison. Despite *WISP* PSF artifact problems, several profiles display scattered/scattered color gradients in the same sense as the scattered/thermal colors, with the UV light more concentrated than the optical at small offsets. Specifically, three of the four stars show a 2200/4400 Å ratio drop for $\phi < 8'$, with 23 Tau's trend being the cleanest and most extensive. 23 Tau has a similar 1650/4400 Å trend, but this is not reproduced by 20 Tau, which has poorer 1650 Å data (see Fig. 12). The 1650 Å-related colors were not reliable for 17 & 25 Tau. No 1650/2200 Å trend is apparent for 20 or 23 Tau.

For an optically thin, foreground nebula, scattered light color gradients indicate changes in the dust phase function asymmetry, $g \equiv \langle \cos\theta \rangle$, where θ is the scattering angle. The 2200/4400 Å trend implies $g(2200) > g(4400)$, and the 23 Tau data suggest $g(1650) > g(4400)$. We cannot evaluate the relationship between $g(2200)$ and $g(1650)$, but the APW fit to foreground 23 Tau nebulosity requires $g(1650) > g(2200) > g(4400)$, and $dg/d\lambda < 0$ for 1550 Å $\leq \lambda \leq$ 5620 Å generally. This trend is consistent with recent grain property estimates (e.g., Gordon, Calzetti, & Witt 1997) and may indicate the "detection" of the small end of the size distribution of dominant scatterers if grains much smaller than λ scatter isotropically and larger grains are strong forward-scatterers (Whittet 1992).

Our color trend conflicts with that of Witt et al. (1986), who found redder UV spectra at smaller ϕ offsets for 17, 20 & 23 Tau and inferred $g(1500) < g(3000)$. Since their pointings have $\phi \leq 1'$, it is possible they sample a small-angle regime of the phase function that behaves differently from that observed by *WISP* and APW, but such ad hoc complexity is not predicted by current grain models. Alternatively, the Witt et al. (1986) data may contain some bias, but we do not attempt to evaluate this here; we simply note their results as opposing ours.

Another source of concern is whether internal reddening could affect the observed color trends. We demonstrate below that it is not significant and also discuss the general redness of the UV/optical colors compared to the stars.

7.2.2. Internal Reddening

To test our assumption that phase function effects dominate the nebular color trends, we estimated the amount of internal reddening produced by a simple smooth dust model constrained by sightline E_{B-V} measurements. The model ignores clumpy dust, which probably has little affect on color gradients. Figure 15 shows the model's uniform, plane-parallel dust slab lying normal to the observer's line of sight to the star, which is a distance d from the observer and a separation s from the slab midplane. A grain in the midplane has offset angle ϕ seen by the observer, scattering angle θ, and offset angle $\theta' = \theta - \phi$ seen by the star, where $s \tan\theta' = (d - s) \tan\phi$. In terms of the line-of-sight depth τ_{LOS}, the optical depth along the light path is

$$\tau_{PATH} \quad = \quad \frac{1}{2}\left(\frac{1}{\cos\theta'} + \frac{1}{\cos\phi}\right)\tau_{LOS} \quad . \tag{1}$$

Since $E_{B-V} \propto \tau$, we can estimate the reddening along the light path relative to the sightline.

The E_{B-V} difference between paths with offsets ϕ_1 and ϕ_2 is that which internal reddening can contribute to observed color gradients. For a Cardelli, Clayton, & Mathis (1989) extinction law, we find the APW 2200/4400 Å color change between $\phi_1 = 5'$ and $\phi_2 = 10'$ requires $\Delta E_{B-V} = 0.077$ for $R_V \equiv A_V/E_{B-V} = 3.1$ and generally $0.065 \leq \Delta E_{B-V} \leq 0.154$ for $2 \leq R_V \leq 6$; Pleiades observations suggest $R_V \sim 3 - 4$ (e.g., Witt, Bohlin, & Stecher 1981; Guthrie 1987). For nebulosity near 23 Tau, which has $E_{B-V} = 0.078$ (Breger 1986), producing this ΔE_{B-V} range requires $61° \leq \theta \leq 74°$ for $5' \leq \phi \leq 10'$ and $R_V = 2$, or $s \sim 0.1$ pc for $d = 130$ pc (Stello & Nissen 2001). Higher, more likely R_V values require higher θ angles and smaller separations, as do lower sightline reddenings. Since 23 Tau has heavier nebulosity and higher sightline reddening than the other bright Pleiades stars, more typical geometric requirements are $\theta \gtrsim 80°$ and $s \lesssim 0.05$ pc.

Though such small separations have been proposed (e.g., Witt et al. 1986), they make shallow intensity slopes harder to explain (§6.2.2), and they contradict ionization balance models that require $s \gtrsim 0.3 - 1.0$ pc in many parts of the nebula (Federman 1982; White 1984). Thus, significant internal reddening gradients seem unlikely. If we assume $s = 0.5$ pc, Breger's (1986) $E_{B-V} = 0.025$ for 25 Tau implies a reddening gradient $\sim 3\%$ that of the APW 2200/4400 Å profile's. Though our 25 Tau colors do not follow the APW line perfectly, they do so well enough to show they are not produced by reddening, and we find similar results for other stars. Consequently, our phase function interpretation in §7.2.1 appears valid.

The face-on, plane-parallel reddening model is simplistic but adequate for these esti-

mations. If the real nebula was flat but tilted, its reddening color gradients might increase significantly at those position angles most tilted toward or away from the observer, but the effect would be less elsewhere, and strong ψ asymmetries in nebular colors are not observed. A large tilt would also displace the point of bluest color from the stellar position, and since this is not seen, any real tilt may be reasonably small. Non-plane-parallel shapes cannot increase internal reddening significantly either. A nebula convex to the observer would produce less reddening than a flat nebula unless its radius of curvature was less than s. A nebula concave to the observer would enhance reddening, but this would not be significant unless it had enough curvature to make the observer's point of view unlikely.

7.2.3. Ultraviolet Faintness

The low *WISP S/N* expresses a poor match of instrumental sensitivity to the UV faintness of the nebula. Though consistent with APW's photometry, this UV faintness remains surprising. None of our UV/optical colors in Figure 14 are systematically bluer than the observed stellar colors. The APW fit for 23 Tau yields $[2200/4400]_{\rm neb} \,/\, [2200/4400]_{\rm star} = 0.75$ at $\phi = 5'$, near *WISP*'s minimum reliable offset. For APW's inner limit of $\phi = 2'.25$, they find a 2200/4400 Å intensity ratio of 1.2 relative to the star. These colors are much redder than simple models would predict.

A smooth, optically thin slab nebula like that discussed in the previous section (see Fig. 15) has colors given by

$$\frac{I_{\lambda_1}(\phi)}{I_{\lambda_2}(\phi)} \;=\; \frac{F_*(\lambda_1)\, C_{_{ext}}(\lambda_1)\, a(\lambda_1)\, \Phi(\theta, \lambda_1)}{F_*(\lambda_2)\, C_{_{ext}}(\lambda_2)\, a(\lambda_2)\, \Phi(\theta, \lambda_2)} \;\;, \tag{2}$$

where F_* is the incident stellar flux, $C_{_{ext}}$ is the dust extinction cross-section, a is the albedo, and Φ is the intensity phase function. If a and $\Phi(\theta)$ are wavelength-independent, the 2200/4400 ratio relative to the star is just $C_{_{ext}}(2200)/C_{_{ext}}(4400)$. This is $3.2 - 1.4$ for $R_V = 2 - 6$, and 2.4 for standard $R_V = 3.1$ extinction (Cardelli et al. 1989); all of these exceed the bluest reliable colors in our data or APW's. But $\Phi(\theta)$ must vary with wavelength (§7.2.2), and the albedo probably does as well.

To examine albedo and phase function effects, we used two grain models: the power-law size distribution of spherical grains developed by Mathis, Rumpl, & Nordsieck (1977; MRN) and explored by White (1979), and the Milky Way dust values assembled from the literature by Gordon et al. (1997; GCW). Table 1 gives MRN & GCW albedo and g values. Both grain models have $a(2200)/a(4400) \simeq 0.78$. If $\Phi(\theta)$ was λ-independent, this albedo ratio

would be just sufficient to match the APW colors at $\phi = 2'.25$ if $R_V \sim 5.4$, but not for larger ϕ or lower R_V. Yet Φ's λ-dependence does not help much if g is restricted to the MRN or GCW values. A Henyey & Greenstein (1941) form for Φ requires $R_V \gtrsim 4$ for either grain model to match APW's $\phi = 2'.25$ colors and higher R_V for larger ϕ, e.g., $R_V > 6$ for $\phi = 5'$.

Our simple slab model is unable to explain the UV faintness of the nebula. The HG phase function has no physical basis, but it's probably a reasonable representation of real grain behavior at the small scattering angles involved here. However, the real dust could have a lower UV albedo than predicted by MRN or GCW, or g(UV) could be higher than predicted. Alternatively, the nebula could be reddened beyond levels expected from E_{B-V} measurements, for example, by small clumps of dust. We consider these possibilities in Paper II.

8. Conclusions

Using *Wide-field Imaging Survey Polarimeter* and Burrell Schmidt telescope observations, we have presented the first wide-field ultraviolet and optical imaging photometry of the Pleiades reflection nebula. Instrumental effects, such as stellar point spread contamination of nebular intensities, required careful processing in both data sets. Despite these complications, our final images are consistent with the photometry of previous studies. The Schmidt data show several features below the sensitivity of photographic surveys and also have the advantage of linearity. The *WISP* maps are not sensitive enough for polarimetry but give valuable photometry of the cluster core nebulosity.

We have examined intensity and color trends near bright Pleiades stars in our *WISP* and Schmidt maps and *IRAS* far-infrared maps. *COBE* results indicate that the *IRAS* data reasonably represent the dust thermal emission. We find the following:

1. In addition to 2-D brightness structure, many intensity profiles show monotonic declines similar to those observed near 23 Tau. The shallow profile slopes may be caused by a significant star-nebula separation, blending of light from many stars, or both.

2. Trends in scattered/thermal intensity ratios show that most of the scattered UV and optical light arises from dust grains in front of the stars. We cannot rule out some dust lying behind the stars, but it does not dominate the scattered light budget.

3. The dust scatters more in the forward direction at ultraviolet than optical wavelengths. Our data lack adequate sensitivity to demonstrate a similar trend between 1650 and 2200 Å, but such a trend is seen in the data of APW.

4. The nebular color gradients are caused by real phase function effects, as they are too large to arise from internal reddening in reasonable scattering geometries.

5. The ultraviolet faintness of the nebula relative to the illuminating stars requires either a significant alteration of dust scattering parameters from standard MRN and GCW grain model values or a larger amount of internal reddening than E_{B-V} measurements dictate.

We pursue quantitative analyses of colors, geometry, and dust with nebular models in Paper II.

It is with great pleasure that we acknowledge the considerable time and assistance provided by P. M. Marcum with Schmidt observations and reduction techniques. In addition, we are very grateful for the many helpful processing comments made by J. S. Gallagher, L. S. Sparke, J. S. Mathis, and A. M. Watson. Considerable software support throughout this project was provided by S. Jansen. A. N. Witt very kindly made the Wesselius memo available to us. E. B. Burgh and the anonymous referee gave a number of helpful comments on the manuscript. We are much indebted to P. Pesch for a generous donation of Schmidt time, and we are also grateful to the NOAO staff for observing assistance on Kitt Peak, and to the staff of Lowell Observatory for their loan of the B_J filter. Special thanks are due to the *WISP* instrument and flight team at the University of Wisconsin Space Astronomy Laboratory for their diligent efforts in making the mission a reality. The Schmidt observations were made with the Burrell Schmidt telescope of the Warner and Swasey Observatory, Case Western Reserve University. *WISP* PSF fitting used the NAG FORTRAN library from the Numerical Algorithms Group. *IRAS* images were generated using the SkyView imaging engine at Goddard Space Flight Center. This research has made use of the Simbad data base, operated at CDS, Strasbourg, France. The *WISP* project is supported by NASA grant NAG5-647 under contract with the University of Wisconsin. SJG wishes to acknowledge additional funding support from the Natural Sciences and Engineering Research Council of Canada.

REFERENCES

Adams, J. D., Stauffer, J. R., Monet, D. G., Skrutskie, M. F., & Beichman, C. A. 2001, AJ, 121, 2053

Allen, M. M., et al. 1997, BAAS, 29, 805 [AAS #190, #24.04]

Andriesse, C.D., Piersma, Th.R., & Witt, A.N. 1977, A&A, 54, 841 (APW)

Arny, T. 1977, ApJ, 217, 83

Bally, J., & White, R. E. 1986, in Proc. Summer School on Interstellar Processes: Abstracts of Contributed Papers, ed. D. J. Hollenbach & H. A. Thronson, Jr. (Washington: NASA TM, 88342), 51

Bohlin, R. C., Hill, J. K., Jenkins, E. B., Savage, B. D., Snow, T. P. Jr., Spitzer, L. Jr., & York, D. G. 1983, ApJS, 51, 277

Bowyer, S. 1991, ARA&A, 29, 59

Breger, M. 1987, ApJ, 319, 754

Breger, M. 1986, ApJ, 309, 311

Cardelli, J. A., Clayton, G. C., & Mathis, J. S. 1989, ApJ, 345, 245

Castelaz, M. W., Sellgren, K., & Werner, M. W. 1987, ApJ, 313, 853

Černis, K. 1987, Ap&SS, 133, 355

Cole, A. A., Nordsieck, K. H., Gibson, S. J., & Harris, W. M. 1999, AJ, 118, 2280

Cole, A. A., Wood, K., & Nordsieck, K. H. 1999, AJ, 118, 2292

Cottrell, M. J., & Witt, A. N. 1983, AJ, 88, 418

Elvius, A., & Hall, J. S. 1967, *Lowell Obs. Bull.*, 7, 17

Federman, S. R. 1982, ApJ, 253, 601

Federman, S. R., & Willson, R. F., 1984, ApJ, 283, 626

Gibson, S. J. 1997, Ph.D. Thesis (U. Wisconsin-Madison); see also Gibson, S. J. 1997, BAAS, 29, 1258 [AAS #191, #32.01]

Gibson, S. J., & Nordsieck, K. H. 2003, ApJ, accepted (Paper II)

Gordon, K. D., Calzetti, D., & Witt, A. N. 1997, ApJ, 487, 625 (GCW)

Gordon, K. J., & Arny, T. T. 1984, AJ, 89, 672

Greenberg, J. M., & Hanner, M. S. 1970, ApJ, 161, 947

Greenberg, J. M., & Roark, T. P. 1967, ApJ, 147, 917

Guhathakurta, P., & Cutri, R. M. 1994, ASP Conf. Ser. 58, *The First Symposium on the Infrared Cirrus and Diffuse Interstellar Clouds*, eds. R. M. Cutri & W. B. Latter, p. 34

Guhathakurta, P., & Tyson, J. A. 1989, ApJ, 346, 773

Gullixson, C. A., Boeshaar, P. C., Tyson, J. A., & Seitzer, P. 1995, ApJS, 99, 281

Guthrie, B. N. G. 1987, QJRAS, 28, 289

Harris, W. M., Nordsieck, K. H., Scherb, F., & Mierkiewicz, E. J. 1999, *Earth, Moon, and Planets*, 78, 161

Henry, R. C. 1991, ARA&A, 29, 89

Henry, R. C., Landsman, W. B., Murthy, J., Tennyson, P. D., Wofford, J. B., & Wilson, R. 1988, *Atlas of the Ultraviolet Sky* (Johns Hopkins University Press)

Henyey, L. G., & Greenstein, J. L. 1941, ApJ, 93, 70

Hildebrand, R. H. 1983, QJRAS, 24, 267

Högbon, J. A. 1974, A&AS, 15, 417

Hubble, E. P. 1922, ApJ, 56, 400

Hurwitz, M., Bowyer, S., & Martin, C. 1991, ApJ, 372, 167

Jura, M. 1979, ApJ, 231, 732

Jura, M. 1977, ApJ, 218, 749

Lagache, G., Abergel, A., Boulanger, F., & Puget, J.-L. 1998, A&A, 333, 709

Landolt, A. U. 1992, AJ, 104, 340

Levasseur-Regourd, A. C., & Dumont, R. 1980, A&A, 84, 277

King, I. R. 1971, PASP, 83, 199

Kormendy, J. 1973, AJ, 78, 255

Mathis, J. S., Rumpl, W., & Nordsieck, K. H. 1977, ApJ, 217, 425 (MRN)

McGlynn, T., Scollick, K., & White, N. 1996, IAU Symp. 179, *New Horizons from Multi-Wavelength Sky Surveys*, eds. B. J. McLean et al., 465

Nordsieck, K. H., & Harris, W. M. 1999, *Proceedings of the Society of Photo-Optical Instrumentation Engineers (SPIE)*, 3764, 124

Nordsieck, K. H., Marcum, P., Jaehnig, K. P., & Michalski, D. E. 1994, *Proceedings of the Society of Photo-Optical Instrumentation Engineers (SPIE)*, 2010, 28

O'Dell, C. R. 1969, ApJ, 156, 381

O'Dell, C. R. 1965, ApJ, 142, 604

Paley, E. S., Low, F. J., McGraw, J. T., Cutri, R. M., & Rix, H.-W. 1991, ApJ, 376, 335

Racine, R. 1996, PASP, 108, 699

Reach, W. T., et al. 1995, ApJ, 451, 188

Röser, S., & Bastian, U. 1988, A&AS, 74, 449

Reynolds, R. J., 1988, AJ, 96, 670

Rush, W. F., & Witt, A. N. 1975, AJ, 80, 31

Schalén, C. 1948, *Ann. Uppsala Obs.*, 2, 5

Schlegel, D. J., Finkbeiner, D. P., & Davis, M. 1998, ApJ, 500, 525

Schoening, W. 1992, *The Burrell-Schmidt Telescope of Case Western Reserve University, Kitt Peak Station CCD Camera Operation Manual* (Tucson: NOAO)

Stello, D., & Nissen, P. E. 2001, A&A, 374, 105

Stetson, P. B. 1987, PASP, 99, 191

Thompson, G. I., Nandy, K., Jamar, C., Monfils, A., Houziaux, L., Carnochan, D. J., & Wilson, R. 1978, *Catalogue of stellar ultraviolet fluxes: A compilation of absolute stellar fluxes measured by the Sky Survey Telescope (S2/68) aboard the ESRO satellite TD-1* (U.K. Science Research Council)

Trapero, J., Welty, D. E., Hobbs, L. M., Lauroesch, J. T., Morton, D. C., Spitzer, L., & York, D. G., 1996, ApJ, 468, 290

van de Hulst, H. C. 1981, *Light Scattering by Small Particles*, Revised Edition (New York: Dover)

Wesselius, P. R. 1980, *Astronomical Netherlands Satellite* internal memorandum 80-43, Space Research Dept., University of Groningen

Wheelock, S. L., et al. 1994, *IRAS* Sky Survey Atlas: Explanatory Supplement (Pasadena: JPL 94-11)

White, R. E. 1984, ApJ, 284, 685

White, R. E., Allen, C. L., Forrester, W. B., Gonnella, A. M., & Young, K. L. 2001, ApJS, 132, 253

White, R. E., & Bally, J. 1993, ApJ, 409, 234

White, R. L. 1979, ApJ, 229, 954

Whittet, D. C. B. 1992, *Dust in the Galactic Environment* (Bristol: IOP)

Witt, A. N. 1985, ApJ, 294, 216

Witt, A. N. 1977, PASP, 89, 750

Witt, A. N., Bohlin, R. C., & Stecher, T. P. 1986, ApJ, 302, 421

Witt, A. N., Bohlin, R. C., & Stecher, T. P. 1981, ApJ, 244, 199

Witt, A. N., & Boroson, T. A. 1990, ApJ, 355, 182

Witt, A. N., Petersohn, J. K., Bohlin, R. C., O'Connell, R. W., Roberts, M. S., Smith, A. M., & Stecher, T. P. 1992, ApJ, 395, L5

Wolff, M. J., Clayton, G. C., & Gibson, S. J. 1998, ApJ, 503, 815

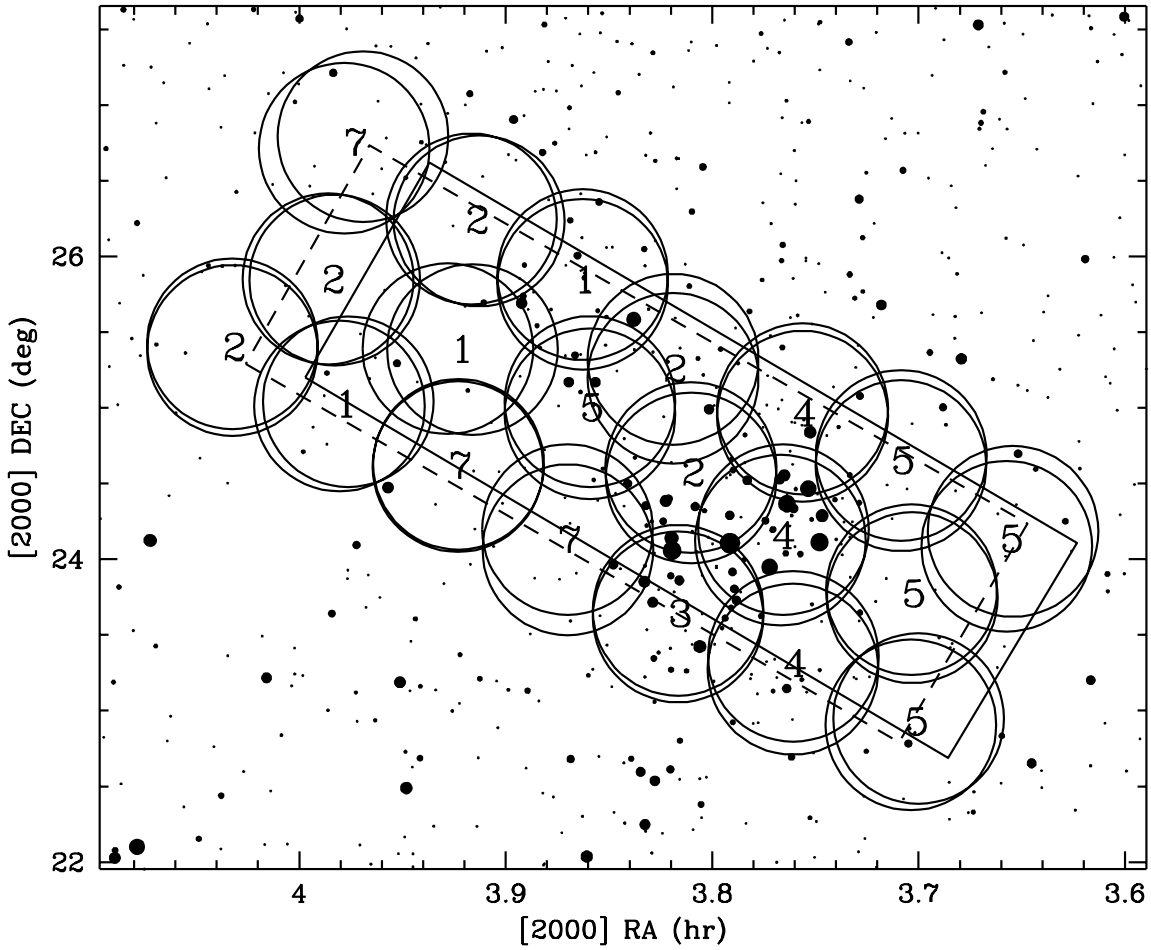

Fig. 1.— The single *WISP* UV field and all 40 Schmidt B_J mosaic fields on the sky. Each Schmidt field is 67.′6 in diameter. The $5^\circ \times 1.7^\circ$ *WISP* field is shown as observed (——) and as originally planned (- - - -). Since the Schmidt survey was carried out first, its fields cover the original *WISP* area. The numbers indicate night of Schmidt observation, where night 1 is 1993 Dec 12. The stars plotted have V magnitudes in the range $3 - 10$.

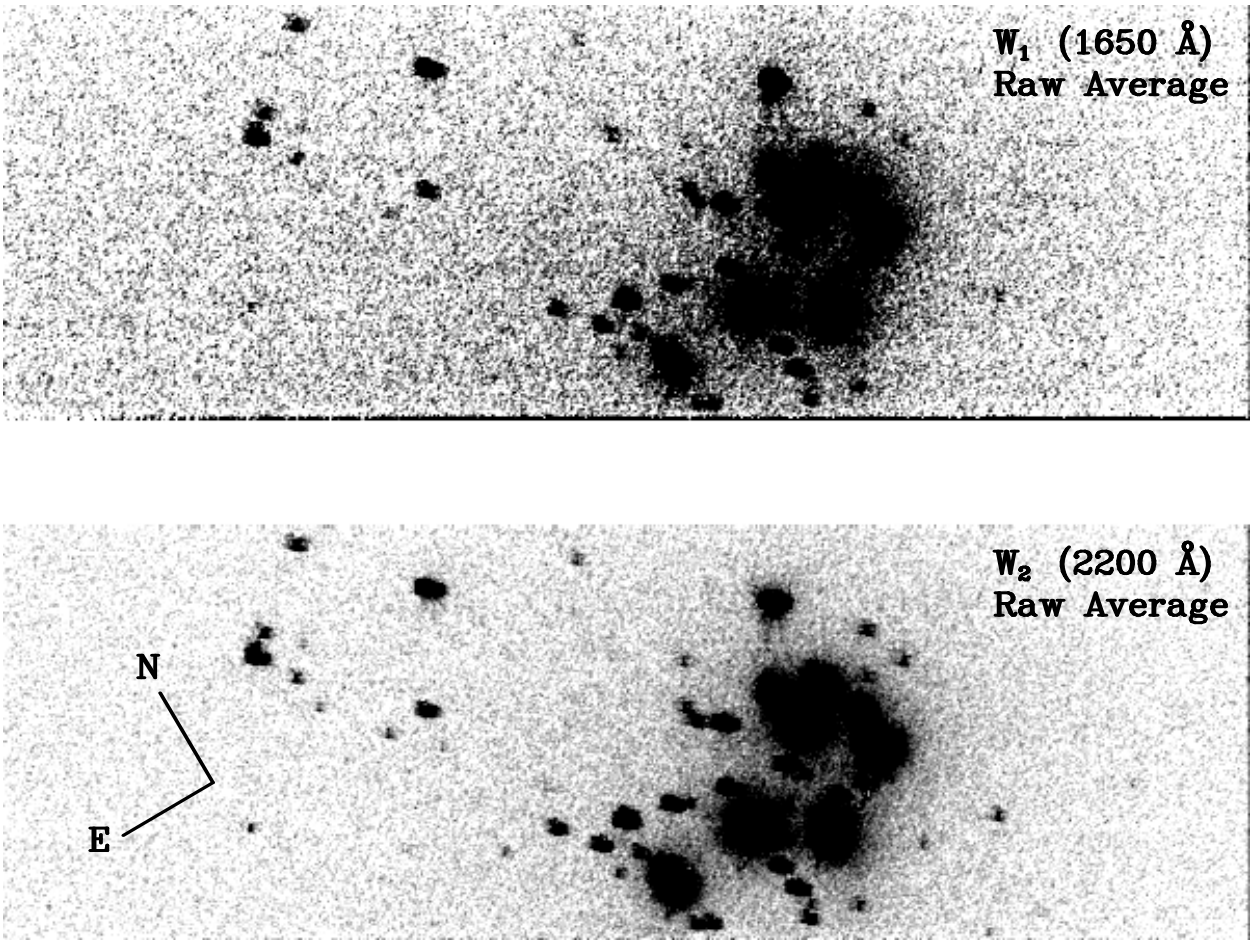

Fig. 2.— W_1 (top) and W_2 (bottom) images prior to PSF subtraction and smoothing. Intensity ranges from 0 (white) to 2.0×10^{-17} erg cm^{-2} s^{-1}Å^{-1}arcsec^{-2} (black). The sky orientations of north and east are indicated.

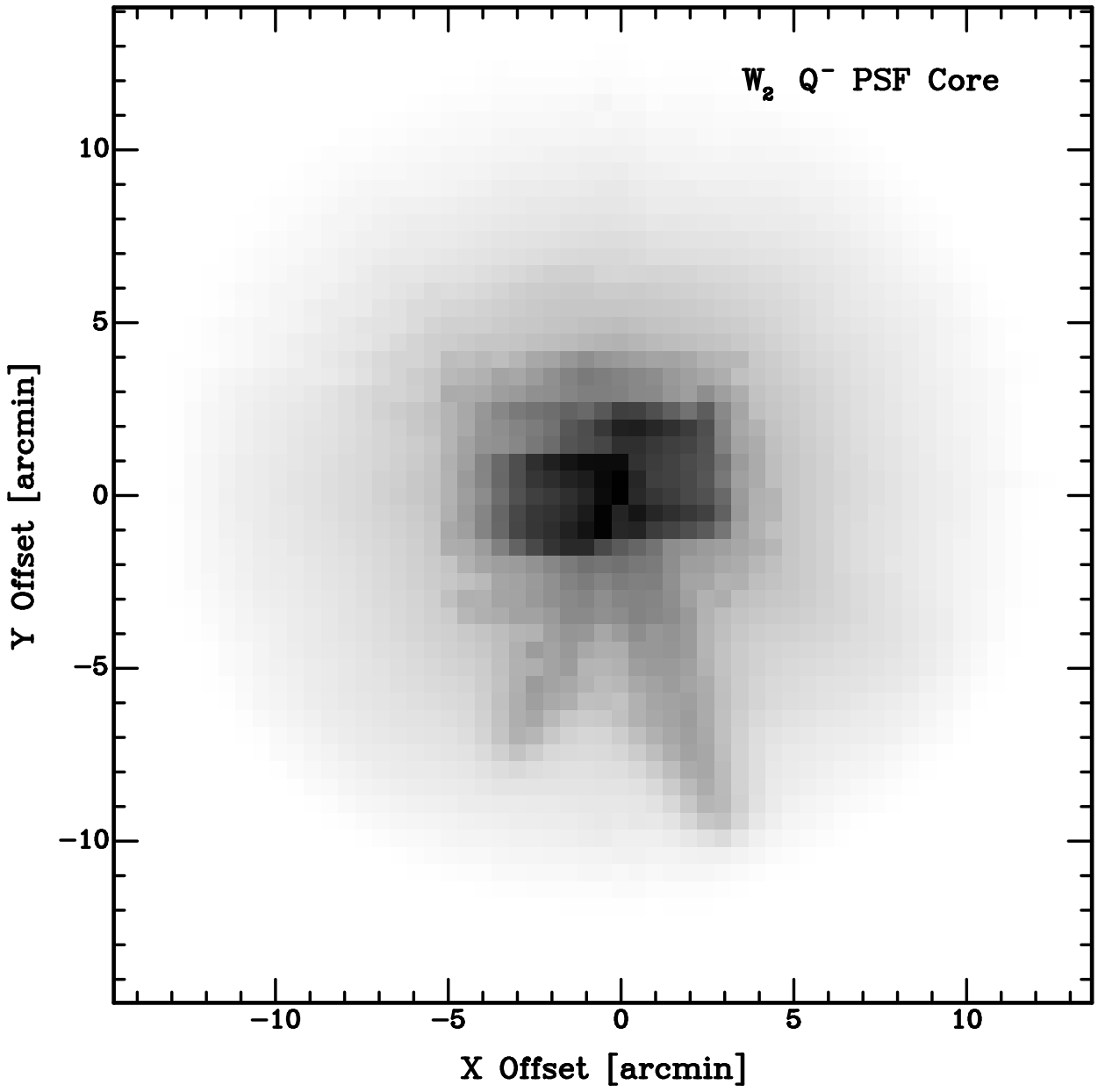

Fig. 3.— W_2 Q^- PSF core region, logarithmic brightness scale (negative). Each pixel is $30''$ across. Outside of the core, the PSF diminishes more smoothly in an approximate power-law aureole.

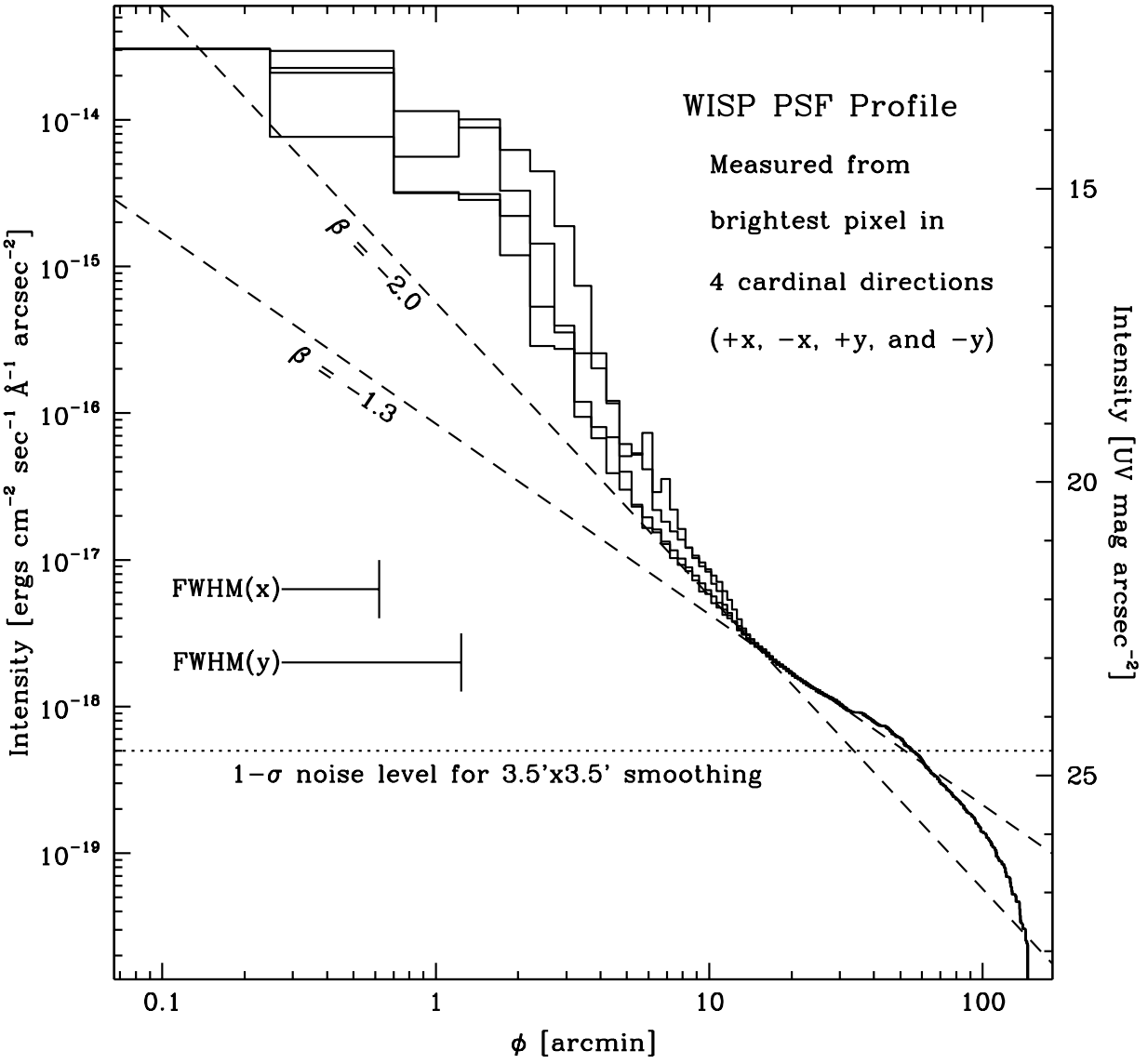

Fig. 4.— W_2 PSF profiles taken left, right, above, and below the brightest PSF pixel and scaled to the brightness of 25 Tau. While the inner PSF is quite complex, the outer aureole exhibits a smooth ϕ^β form out to the noise limit at $\phi \sim 60'$, with $-1.3 \geq \beta \geq -2$.

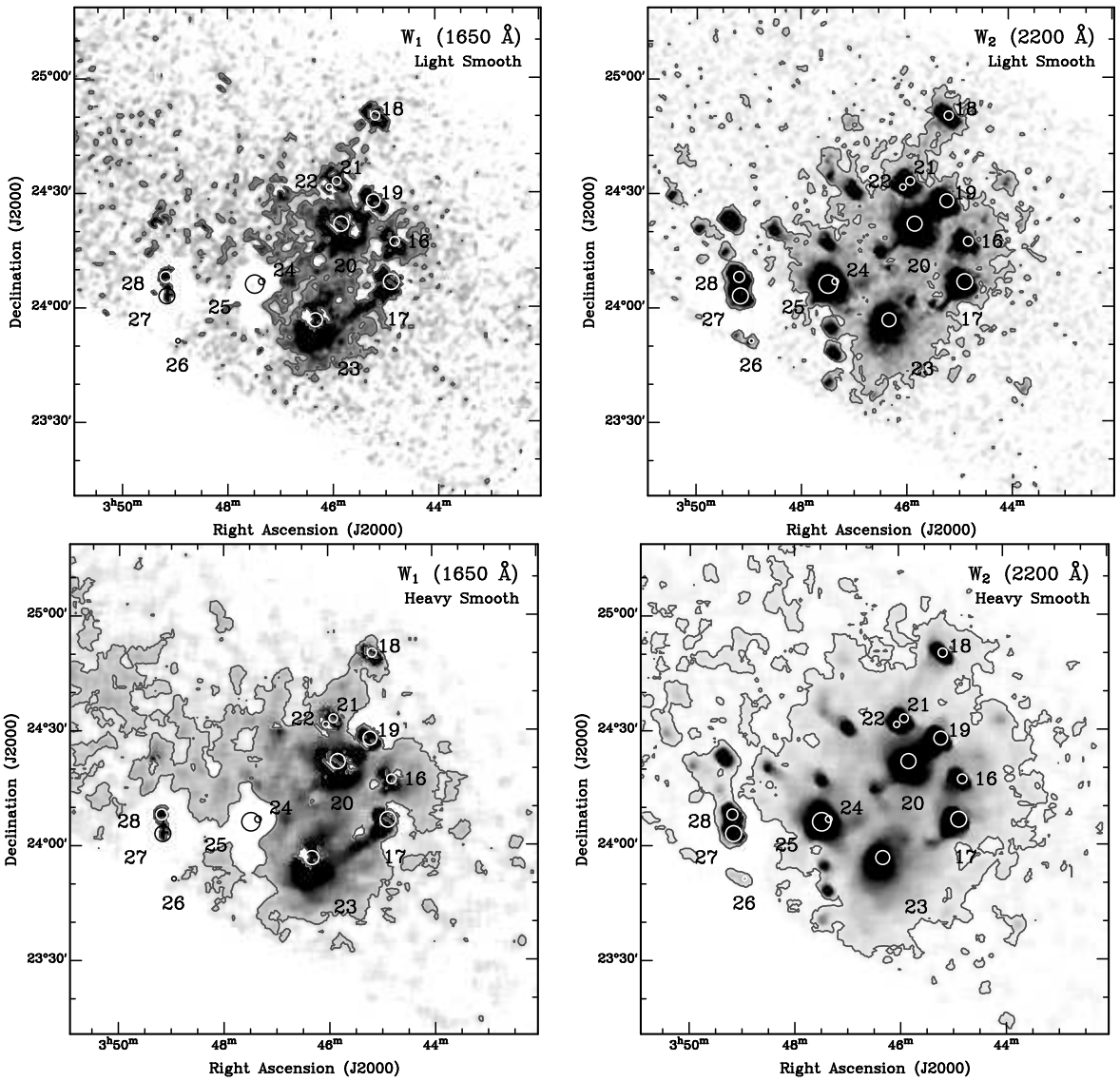

Fig. 5.— W_1 (left) and W_2 (right) images after PSF subtraction, with $1\farcm5 \times 1\farcm5$ (top) and $3\farcm5 \times 3\farcm5$ (bottom) smoothing to reduce noise. Intensity scaling is identical to Fig. 2. The gray contour encloses data with $S/N > 3$, based on read, dark, and photon noise and a 4% flux scaling error (§2.2). Flamsteed catalog stars are numbered.

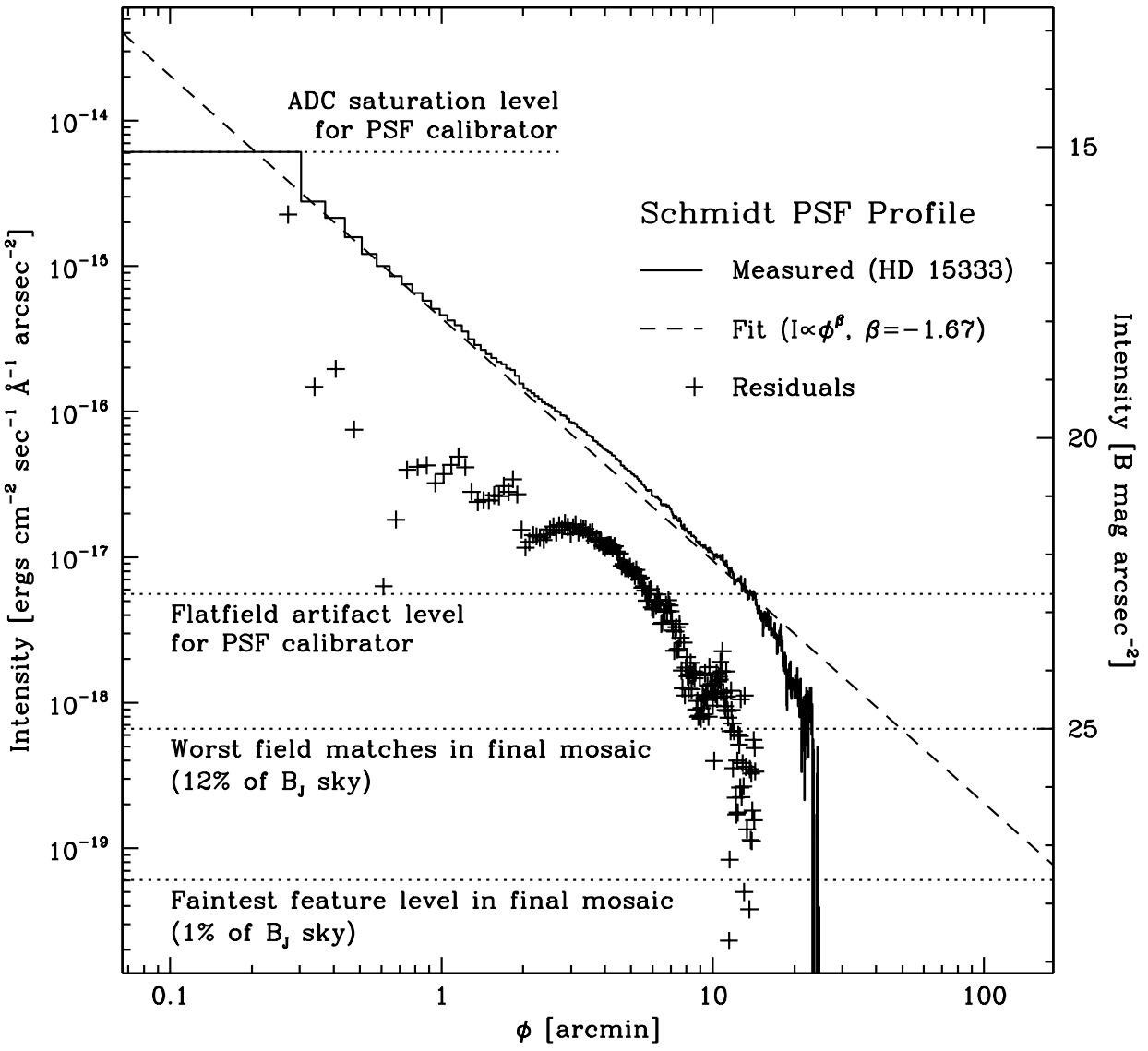

Fig. 6.— Schmidt PSF profile of the B=6.8 magnitude star HD 15333, rescaled to the B=2.8 brightness of 25 Tau. A ϕ^{β} fit constructed not to exceed good data values is given, with $\beta = -1.67$. This power law was extrapolated to larger offset angles for the subtraction of PSFs of bright Pleiades stars.

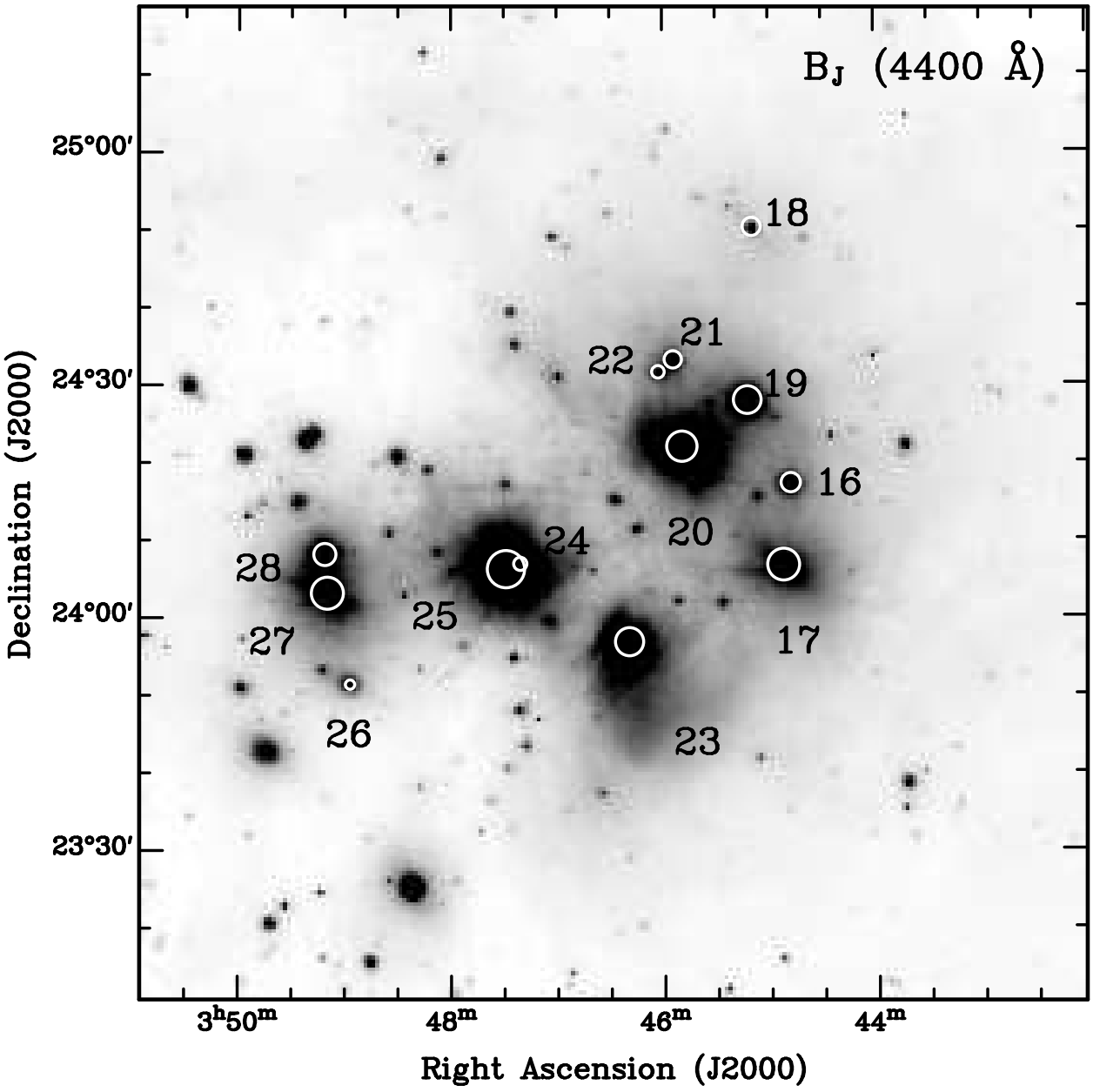

Fig. 7.— Schmidt mosaic image of the cluster core. Intensity scaling, coverage, and labeling are as in Fig. 5.

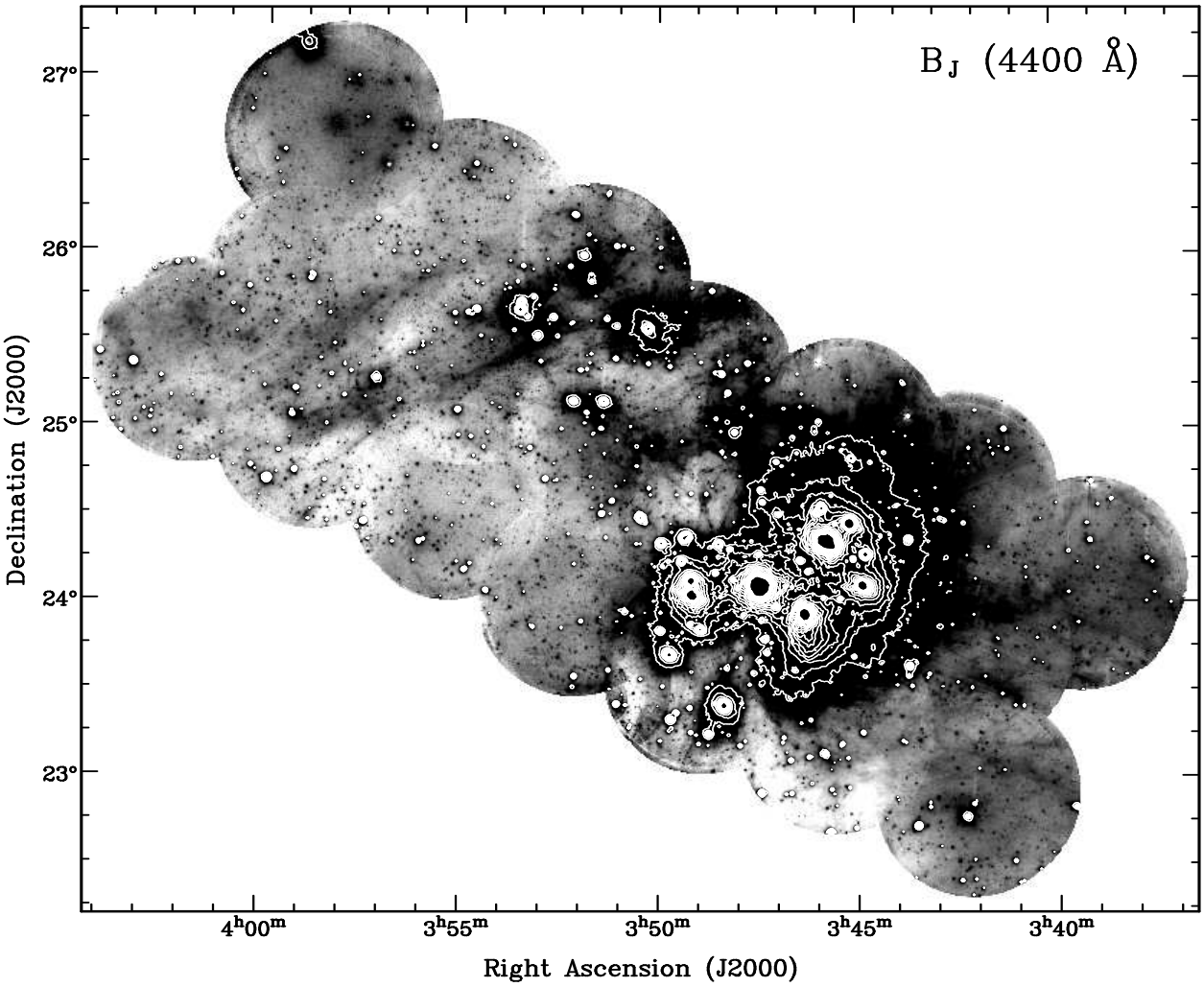

Fig. 8.— Full Schmidt mosaic. Intensity ranges linearly from 0.0 (white) to 1.0×10^{-18} erg cm^{-2} s^{-1}Å^{-1}arcsec^{-2} = 24.5 B mag arcsec^{-2} (black) to emphasize the faint outer nebulosity. Brighter regions are marked with white contours every 2.0×10^{-18} erg cm^{-2} s^{-1}Å^{-1}arcsec^{-2}, up to 4.0×10^{-17} erg cm^{-2} s^{-1}Å^{-1}arcsec^{-2} = 20.5 B mag arcsec^{-2}.

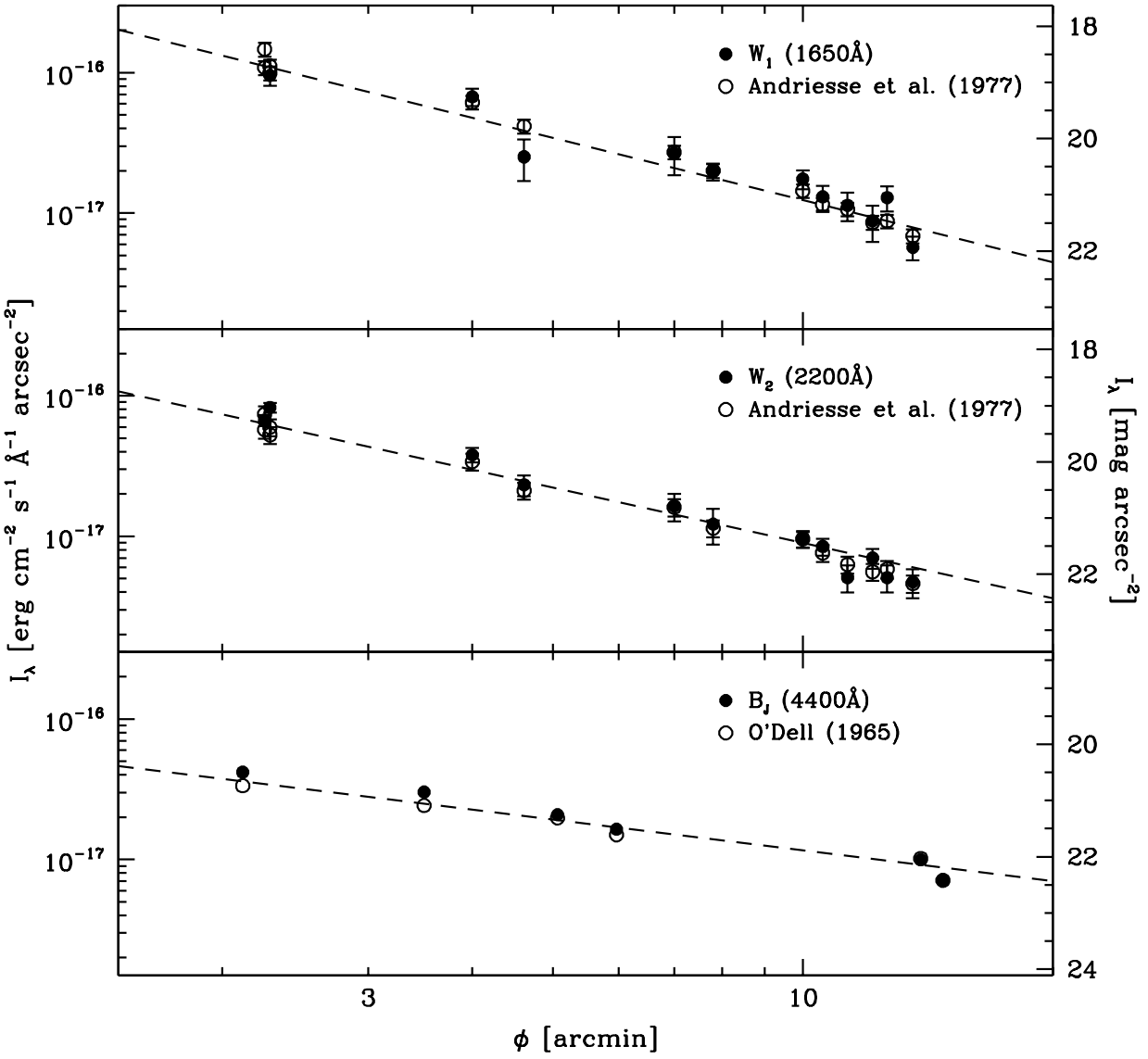

Fig. 9.— *WISP* & Schmidt vs. previous photometry of the Merope Nebula. Filled circles are new data. Open circles are from APW and O'Dell (1965). Error bars show 1σ uncertainty ranges in the UV data; these are too small to plot at 4400 Å. The dashed lines indicate APW's power-law fits to the nebular brightness. All three intensity ranges are the same. Magnitude scale differences arise from varied zero-point definitions.

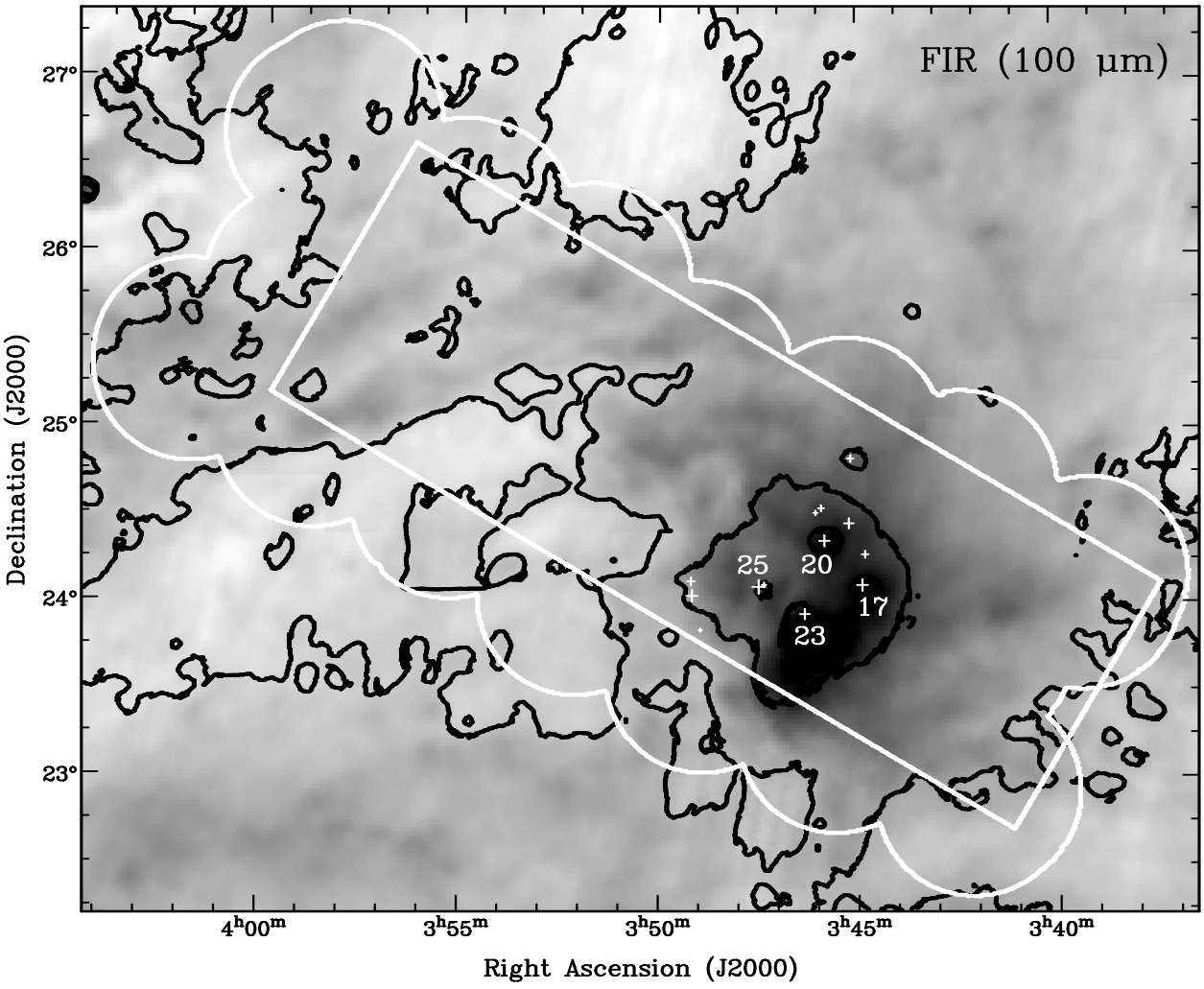

Fig. 10.— IRAS 100 μm intensity on a log scale ranging from 3 (white) to 100 MJy sr^{-1} (black). Black contours mark 60/100 μm color temperatures of 20, 25, and 30 K. Dust in the cluster core has $T \gtrsim 25$ K, and $T > 30$ K is reached near 17, 20, 23 and 25 Tau. All Pleiads with Flamsteed numbers are marked with crosses. Outlines of *WISP* and Schmidt field coverages are given for reference.

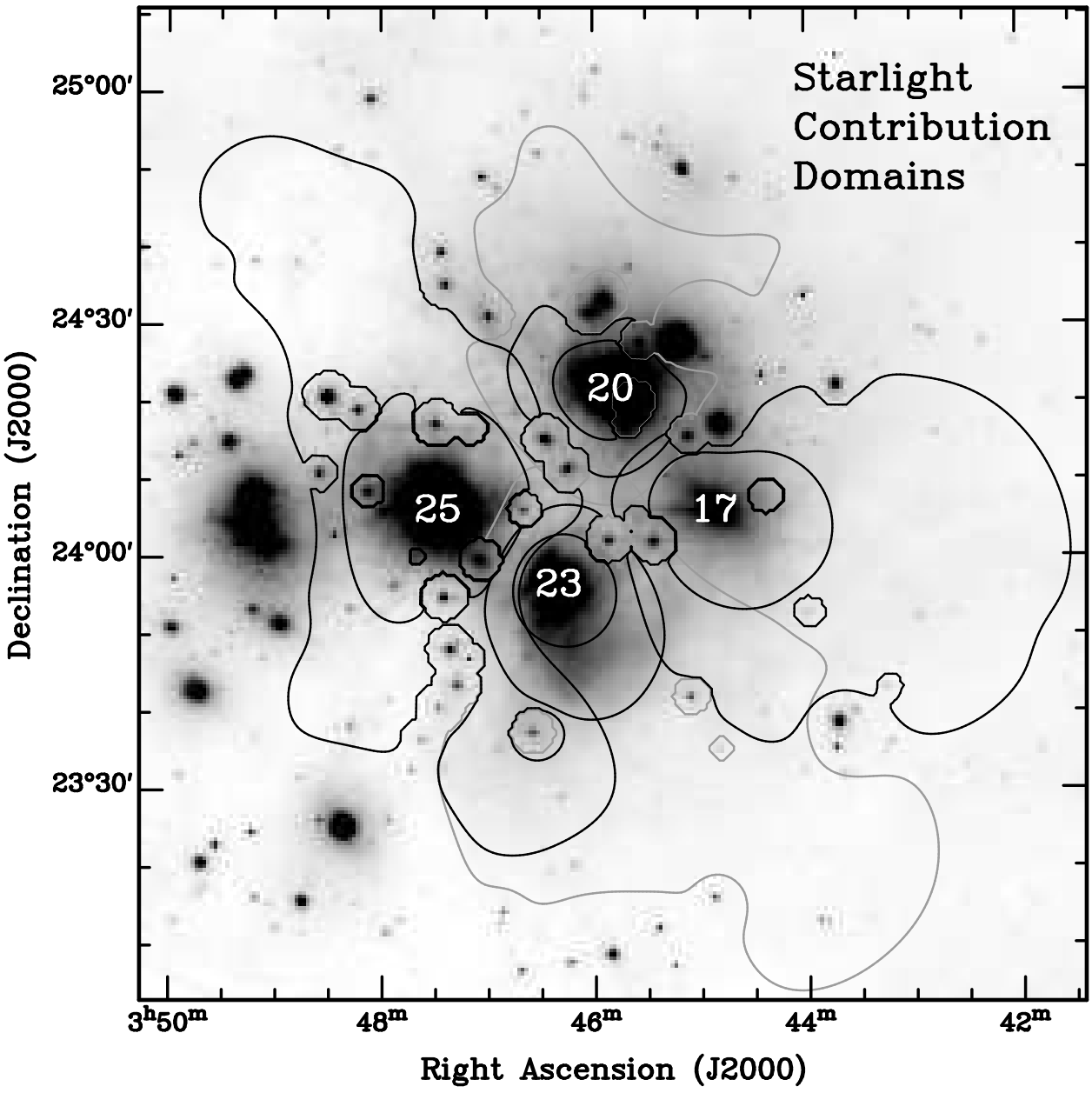

Fig. 11.— Areas from which radial intensity and color profiles were extracted for 17, 20, 23, and 25 Tau. Each star's "domain" is traced by black contours showing 50% and 25% contributions to the total light incident on the grains for a simple geometry (§6.1). Lower contributions at the 15% level for 20 Tau and the 10% level for 23 Tau are also shown. The underlying negative image is Schmidt B_J intensity.

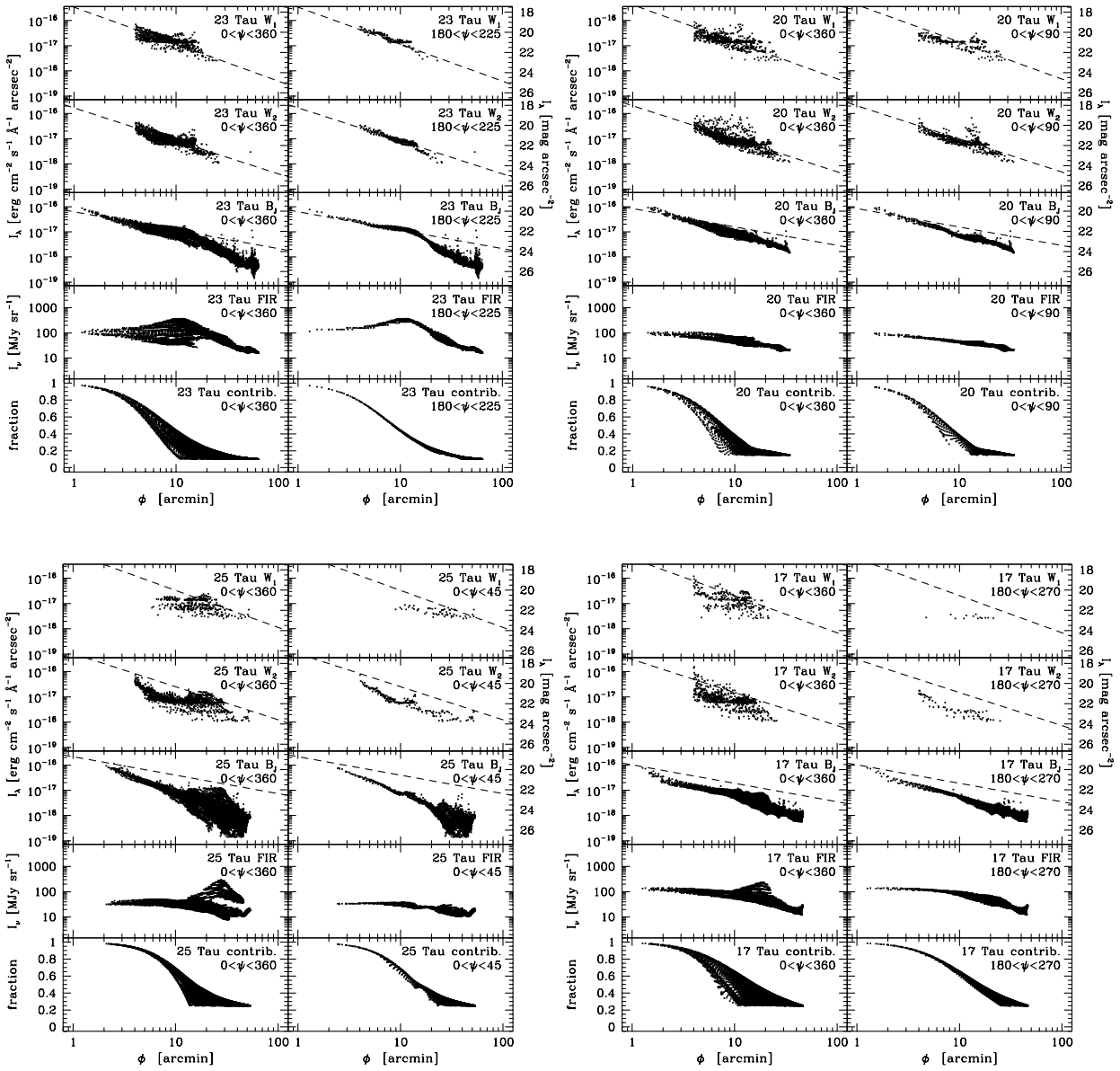

Fig. 12.— Radial intensity profiles for: (*a*) 23, (*b*) 20, (*c*) 25, and (*d*) 17 Tau, extracted from the areas indicated in Fig. 11. Dashed lines mark the APW intensity fit to 23 Tau, rescaled to other stellar fluxes for comparison. Left-side panels show complete pixel sets, while those on the right plot subsets in azimuth. The estimated fraction of incident light contributed by each star is also shown. See §6.1 for full details.

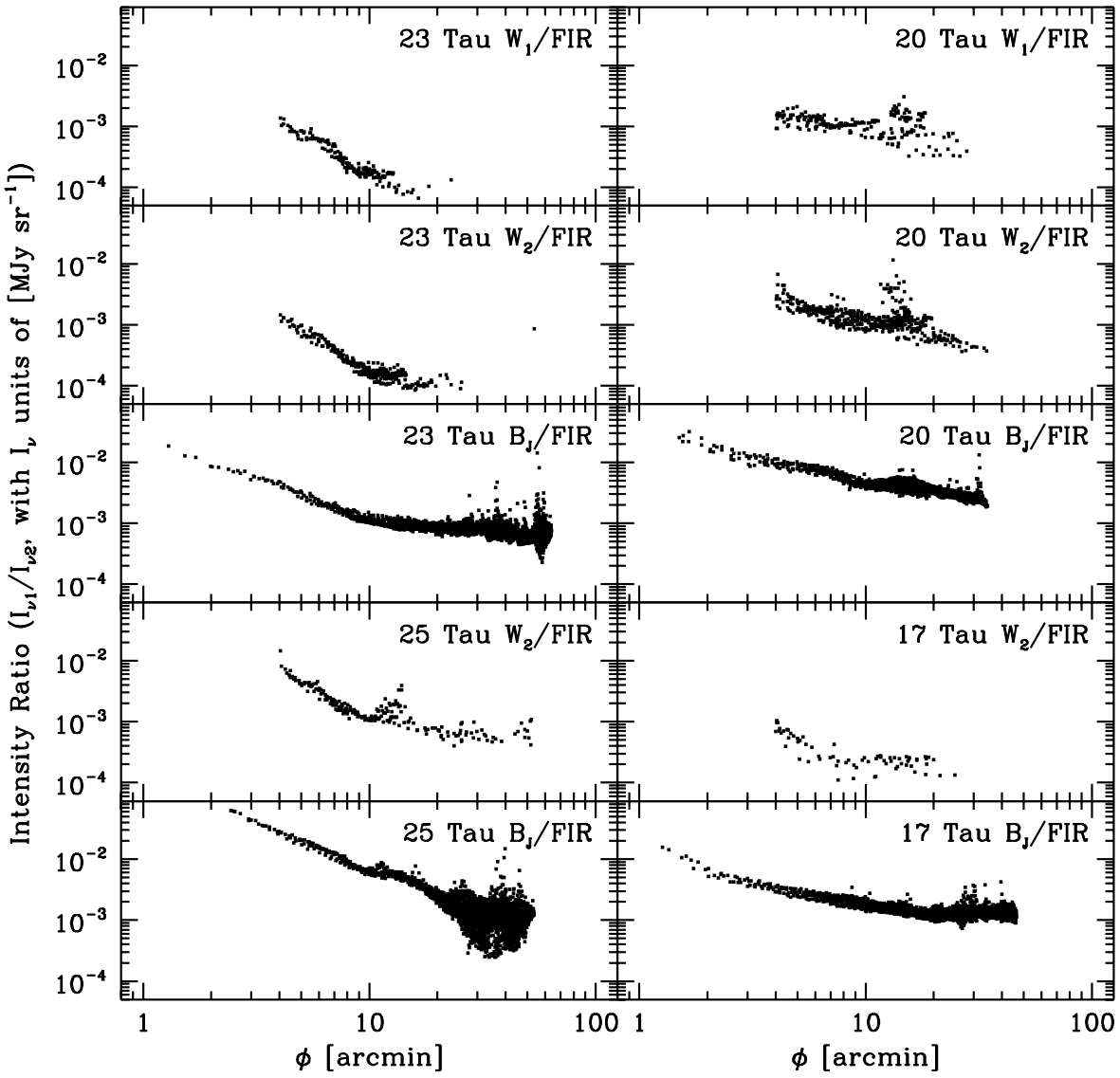

Fig. 13.— Radial scattered/thermal color profiles for 23, 20, 25 and 17 Tau using the same azimuthal subsets as the right-side panels in Fig. 12. W_1 PSF artifacts for 25 & 17 Tau contaminated the W_1/FIR colors of nebulosity near those stars.

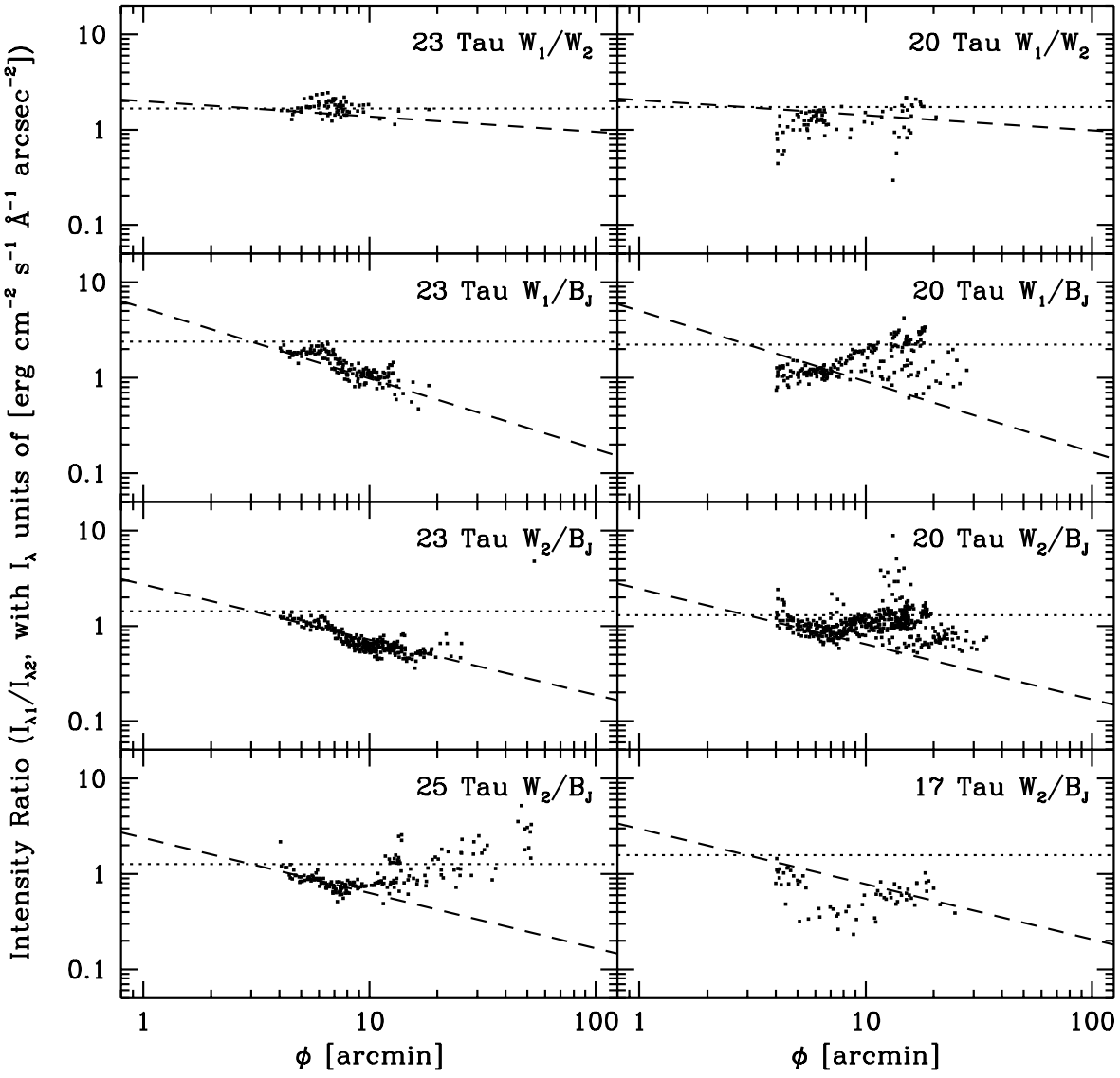

Fig. 14.— Radial scattered/scattered color profiles for 23, 20, 25 and 17 Tau using the same azimuthal subsets as the right-side panels in Fig. 12. W_1-related colors near 17 & 25 Tau are unreliable. Dashed lines mark the APW color fit to 23 Tau, rescaled to other stellar colors for comparison. Dotted lines indicate apparent stellar colors, uncorrected for interstellar reddening.

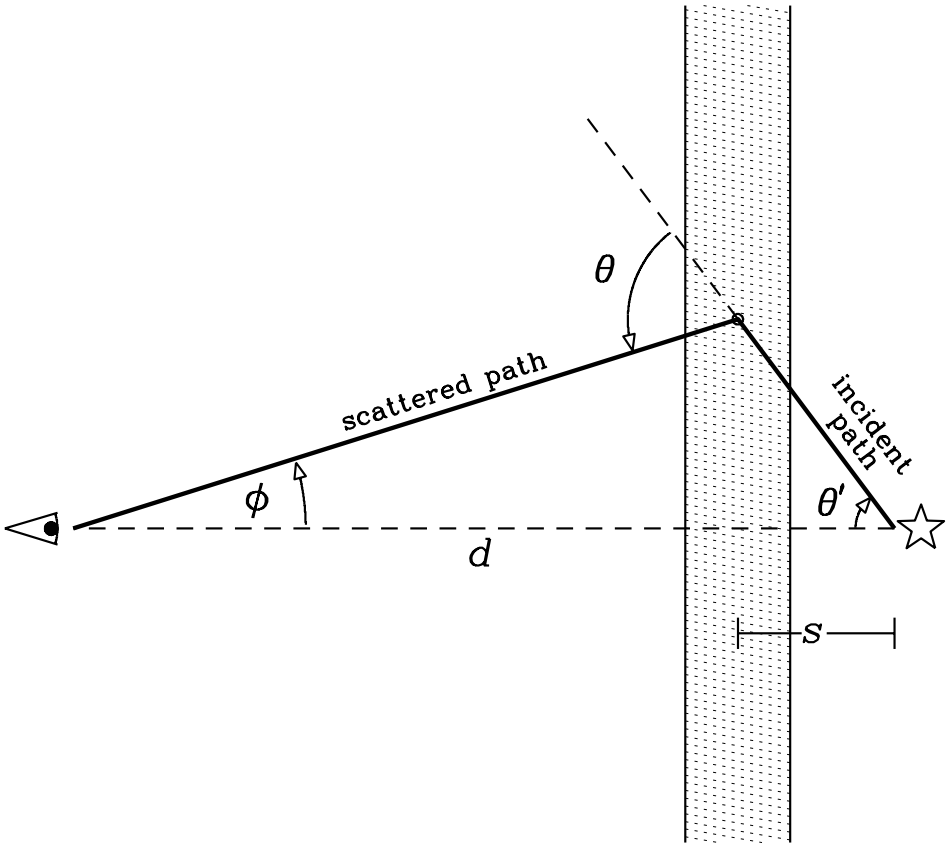

Fig. 15.— A simple homogeneous slab geometry useful for considering reddening effects. See §7.2.2 for details.

Table 1. Grain Model Properties

		MRN[†]		GCW[‡]	
Filter	λ	albedo	g	albedo	g
W_1	1650 Å	0.45	0.61	0.66	0.74
W_2	2200 Å	0.52	0.48	0.47	0.71
B_J	4400 Å	0.66	0.52	0.61	0.63

[†]Values from Mathis et al. (1977) and White (1979).

[‡]Values from Gordon et al. (1997).